Supplementary Materials for

A general method to synthesize and sinter bulk ceramics in seconds

Chengwei Wang, Weiwei Ping, Qiang Bai, Huachen Cui, Ryan Hensleigh, Ruiliu Wang, Alexandra H. Brozena, Zhenpeng Xu, Jiaqi Dai, Yong Pei, Chaolun Zheng, Glenn Pastel, Jinlong Gao, Xizheng Wang, Howard Wang, Ji-Cheng Zhao, Bao Yang, Xiaoyu (Rayne) Zheng*, Jian Luo*, Yifei Mo*, Bruce Dunn, Liangbing Hu*

*Corresponding author. Email: binghu@umd.edu (L.H.); yfmo@umd.edu (Y.M.); raynexzheng@vt.edu (X.Z.); jluo@ucsd.edu (J.L.)

Published 1 May 2020, *Science* **368**, 521 (2020)
DOI: 10.1126/science.aaz7681

This PDF file includes:

Materials and Methods
Supplementary Text
Figs. S1 to S32
Tables S1 to S3
Captions for Movies S1 and S2
References

Other Supplementary Material for this manuscript includes the following:
(available at science.sciencemag.org/content/368/6490/521/suppl/DC1)

Movies S1 and S2 (.mp4)

Table of Contents

Materials and Methods 4
Setup of the ultrafast high-temperature sintering (UHS) process 4
Preparation of ceramic materials by the UHS technique 4
Preparation of the garnet-based SSEs with a conventional furnace. 4
List of the UHS-sintered ceramics 5
Li7-Garnet-based solid-state electrolytes 5
10 compositions for co-sintering demonstrations in Figure 3F 8
Ceramics with high sintering temperatures 9
Non-garnet-based solid-state electrolytes 9
Mixed ionic-electric conductor 9
Preparation of the co-sintered all solid-state batteries 9
Materials characterization 9
Electrochemical measurements 10
Neutron depth profiling (NDP) measurements 10
Simulations of temperature distribution in sample pellet during UHS process 10
Table S1. Geometry Parameters Used in the Numeric Model 11
Table S2. Material properties Used in the Numeric Model 11
First-principles calculations 13
Material synthesis and fabrication of the 3D-printed SiOC structures 14
Calibration of the magnetic flux density sensor 15
Supporting Figures 18
Figure S1: Temperature contours of the LLZTO pellet for the six simulation cases (A1-A6) 18
Figure S2. UV-Vis spectrum of the UHS carbon heaters for temperature measurement 19
Figure S3. Typical temperature profile of conventional furnace sintering techniques 20
Figure S4. Comparison of different sintering methods 21
Table S3. Typical parameters of different rapid sintering methods 22
Figure S5. Relationship of relative density and grain size with sintering time for LLZTO at three different isothermal holding temperatures. 23
Figure S6. (A)TOF-SIMS mapping of Li, La, Zr, and O elements at different depths across the thickness of the sintered garnet pellet from one surface to the other surface. 26
Figure S7. Schematic Time-Temperature-Transformation diagram of LLZTO garnet 28
Figure S8. Comparison of UHS and regular sintering of LLZTO garnet materials. 29
Figure S9. Typical EIS measurement of the UHS-sintered garnet SSE, made with a sintering temperature of 1,500 ℃ for 10 s 31
Figure S10. XRD Patterns of the LATP ($Li_{1.3}Al_{0.3}Ti_{1.7}(PO_4)_3$), LLTO ($Li_{0.3}La_{0.567}TiO_3$), Al_2O_3, and YSZ made by UHS sintering 32
Figure S11. SEM image of the UHS-sintered Al_2O_3 pellet 33
Figure S12. SEM image of the UHS-sintered Yttria-stabilized ZrO_2 (YSZ) 34
Figure S13. SEM image of the UHS-sintered $Li_{1.3}Al_{0.3}Ti_{1.7}(PO_4)_3$ (LATP) 35
Figure S14. SEM image of the UHS-sintered $Li_{0.3}La_{0.567}TiO_3$ (LLTO). 36
Figure S15. The XPS spectra of the main elements in pellets of LLZTO, LLTO, YSZ, and Al_2O_3 sintered by UHS 37
Figure S16. Ellingham diagram. 40
Figure S17. XRD of the UHS-synthesized $LiCoO_2$ from Li_2CO_3 and Co_3O_4 precursors at a temperature of 1,000 ℃. 42

Figure S18. SEM images of the UHS-sintered $Li_7Pr_3Zr_2O_{12}$ (LPrZO) garnet pellet 43
Figure S19. SEM images of the UHS-sintered $Li_{6.5}Sm_3Sn_{1.5}Ta_{0.5}O_{12}$ (LSmSnTO) garnet pellet. 44
Figure S20. SEM images of the UHS-sintered $Li_7Nd_3Sn_2O_{12}$ (LNdSnO) garnet pellet 45
Figure S21. SEM images of the UHS-sintered $Li_{6.5}Sm_3Zr_{1.5}Ta_{0.5}O_{12}$ (LSmZTO) garnet pellet. . 46
Figure S22. SEM images of the UHS-sintered $Li_{6.5}Nd_3Zr_{1.5}Ta_{0.5}O_{12}$ (LNdZTO) garnet pellet. .. 47
Figure S23. XRD patterns of the newly predicted garnet materials synthesized by the UHS technique directly from the material precursors in one step 48
Figure S24. Electrochemical performance of the UHS-sintered LNdZTO ($Li_{6.5}Nd_3Zr_{1.5}Ta_{0.5}O_{12}$) garnet with a thickness of 0.5 mm 49
Figure S25. UHS-sintered unstable garnet composition predicted by computation. 50
Figure S26. Electrochemical performance of the UHS-sintered LLZTO garnet SSE 51
Figure S27. Cycling stability of the Li-UHS-sintered LLZTO-Li symmetric cell 53
Figure S28. The stable electrochemical windows of lithium ionic conductors 55
Figure S29. An LATP-coated LLZTO bilayer SSE sintered in a conventional furnace at 1,200 ℃ for 1 h 56
Figure S30. Li_3PO_4-LLZTO ($Li_{6.5}La_3Zr_{1.5}Ta_{0.5}O_{12}$) glass-ceramic composite achieved by the UHS technique without side reactions due to the short sintering time (10 s) 57
Figure S31. The UHS-sintered 3D printed multi-material magnetic flux density sensor 58
Figure S32. Photographs of carbon heater for conformal sintering 60
Supplementary Movie Legends 61
Movie S1. Typical UHS process for rapid synthesis and sintering of LLZTO garnet SSE 61
Movie S2. Typical UHS process for rapid synthesis and sintering of 3D printed SiOC 61
References .....

Materials and Methods

Setup of the ultrafast high-temperature sintering (UHS) process

The Joule heating elements were composed of two parallel strips of carbon paper (Fuel Cell Earth) that were 10 cm in length and 1-2 cm wide, which we suspended and attached to the edges of glass slides by silver paste (SPI Supplies) and conductive copper tape. A VOLTEQ HY6020EX was used as the DC power source with tunable current (0–20 A) and voltage (0–50 V). The temperature of the heater was calculated from the UV-Vis spectra measured with a Vision Research Phantom Miro M110 high-speed camera with an error bar of about ± 100 ℃.

Preparation of ceramic materials by the UHS technique

The raw materials were stoichiometrically mixed by ball-milling in isopropyl alcohol for 12 h. After drying at 200 ℃, the precursor powders were pressed into pellets with a die and then directly sintered to ceramic pellets via the ultrafast high-temperature sintering (UHS) technique for less than 10 s. All-UHS processes were conducted in an Ar-filled glovebox. The heating rate and temperature of the heater were precisely controlled by tuning the current (~10-20 A) of the DC power. For the garnet-based solid-state electrolytes (SSEs), the sintered pellets were polished and stored in a glovebox for electrochemical tests.

Preparation of the garnet-based SSEs with a conventional furnace.

The conventional solid-phase sintering process was conducted in a box furnace with the same compositions and excess Li where appropriate. An additional powder bed was used to compensate for the Li loss during the regular furnace synthesis. The control pellets for Li loss studies were sintered at 1,200 ℃ in a furnace for 10 h.

List of the UHS-sintered ceramics

Li7-Garnet-based solid-state electrolytes

Li7-garnets have the formula of $Li_7A_3B_2O_{12}$ (A = La Group, B = Mo, W, Sn, Zr). The typical dopants studied in this work were 0.25 Al and 0.25 Ga in the Li-site or 0.5 Ta in the B-site. For example, LLZO was $Li_7La_3Zr_2O_{12}$, while LLZTO was $Li_{6.5}La_3Zr_{1.5}Ta_{0.5}O_{12}$.

LLZO and LLZTO were sintered from stoichiometrically mixed raw materials of Li_2CO_3 (99.9%, Sigma Aldrich), La_2O_3 (≥ 99.9%, Sigma Aldrich), ZrO_2 (99.9%, Sigma Aldrich), and Ta_2O_5 (99.9%, Sigma Aldrich), with 10% excess Li.

$Li_6Al_{0.25}La_3Zr_{1.75}Ta_{0.25}O_{12}$ was sintered from stoichiometrically mixed raw materials of Li_2CO_3 (99.9%, Sigma Aldrich), Al_2O_3 (99.9%, Sigma Aldrich), La_2O_3 (≥ 99.9%, Sigma Aldrich), ZrO_2 (99.9%, Sigma Aldrich), and Ta_2O_5 (99.9%, Sigma Aldrich), with 10% excess Li.

$Li_{6.25}Al_{0.25}La_3Zr_2O_{12}$ was sintered from stoichiometrically mixed raw materials of Li_2CO_3 (99.9%, Sigma Aldrich), Al_2O_3 (99.9%, Sigma Aldrich), La_2O_3 (≥ 99.9%, Sigma Aldrich), and ZrO_2 (99.9%, Sigma Aldrich), with 10% excess Li.

$Li_{6.25}Ga_{0.25}La_3Zr_2O_{12}$ was sintered from stoichiometrically mixed raw materials of Li_2CO_3 (99.9%, Sigma Aldrich), Ga_2O_3 (99.9%, Sigma Aldrich), La_2O_3 (≥ 99.9%, Sigma Aldrich), and ZrO_2 (99.9%, Sigma Aldrich), with 10% excess Li.

LGdZO was sintered with the chemical formula of $Li_7Gd_3Zr_2O_{12}$ from stoichiometrically mixed raw materials of Li_2CO_3 (99.9%, Sigma Aldrich), Gd_2O_3 (99.9%, Sigma Aldrich), ZrO_2 (99.9%, Sigma Aldrich), and Ta_2O_5 (99.9%, Sigma Aldrich), with 10% excess Li.

LYbZO was sintered with the chemical formula of $Li_7Yb_3Zr_2O_{12}$ from stoichiometrically mixed raw materials of Li_2CO_3 (99.9%, Sigma Aldrich), Yb_2O_3 (99.9%, Sigma Aldrich), ZrO_2 (99.9%, Sigma Aldrich), and Ta_2O_5 (99.9%, Sigma Aldrich), with 10% excess Li.

LNdZO and LNdZTO were sintered with the chemical formula of $Li_7Nd_3Zr_2O_{12}$ and $Li_{6.5}Nd_3Zr_{1.5}Ta_{0.5}O_{12}$ from stoichiometrically mixed raw materials of Li_2CO_3 (99.9%, Sigma Aldrich), Nd_2O_3 (99.9%, Sigma Aldrich), ZrO_2 (99.9%, Sigma Aldrich), and Ta_2O_5 (99.9%, Sigma Aldrich), with 10% excess Li.

LPrZO and LPrZTO were sintered with the chemical formula of $Li_7Pr_3Zr_2O_{12}$ and $Li_{6.5}Pr_3Zr_{1.5}Ta_{0.5}O_{12}$ from stoichiometrically mixed raw materials of Li_2CO_3 (99.9%, Sigma Aldrich), Pr_6O_{11} (99.9%, Sigma Aldrich), ZrO_2 (99.9%, Sigma Aldrich), and Ta_2O_5 (99.9%, Sigma Aldrich), with 10% excess Li.

LSmZO and LSmZTO were sintered with the chemical formula of $Li_7Sm_3Zr_2O_{12}$ and $Li_{6.5}Sm_3Zr_{1.5}Ta_{0.5}O_{12}$ from stoichiometrically mixed raw materials of Li_2CO_3 (99.9%, Sigma Aldrich), Sm_2O_3 (99.9%, Sigma Aldrich), ZrO_2 (99.9%, Sigma Aldrich), and Ta_2O_5 (99.9%, Sigma Aldrich), with 10% excess Li.

LLSnO and LLSnTO were sintered with the chemical formula of $Li_7La_3Sn_2O_{12}$ and $Li_{6.5}La_3Sn_{1.5}Ta_{0.5}O_{12}$ from stoichiometrically mixed raw materials of Li_2CO_3 (99.9%, Sigma Aldrich), La_2O_3 (99.9%, Sigma Aldrich), SnO_2 (99.9%, Sigma Aldrich), and Ta_2O_5 (99.9%, Sigma Aldrich), with 10% excess Li.

LNdSnO and LNdSnTO were sintered with the chemical formula of $Li_7Nd_3Sn_2O_{12}$ and $Li_{6.5}Nd_3Sn_{1.5}Ta_{0.5}O_{12}$ from stoichiometrically mixed raw materials of Li_2CO_3 (99.9%, Sigma

Aldrich), Nd_2O_3 (99.9%, Sigma Aldrich), SnO_2 (99.9%, Sigma Aldrich), and Ta_2O_5 (99.9%, Sigma Aldrich), with 10% excess Li.

LSmSnO and LSmSnTO were sintered with the chemical formula of $Li_7Sm_3Sn_2O_{12}$ and $Li_{6.5}Sm_3Sn_{1.5}Ta_{0.5}O_{12}$ from stoichiometrically mixed raw materials of Li_2CO_3 (99.9%, Sigma Aldrich), Sm_2O_3 (99.9%, Sigma Aldrich), SnO_2 (99.9%, Sigma Aldrich), and Ta_2O_5 (99.9%, Sigma Aldrich), with 10% excess Li.

10 compositions for co-sintering demonstrations in Figure 3F

$Li_{6.5}La_3Zr_{1.5}Ta_{0.5}O_{12}$+10% Li_3PO_4

$Li_6Al_{0.25}La_3Zr_{1.75}Ta_{0.25}O_{12}$

$Li_{6.25}Al_{0.25}La_3Zr_2O_{12}$

$Li_{6.25}Ga_{0.25}La_3Zr_2O_{12}$

$Li_{6.5}La_3Zr_{1.5}Ta_{0.5}O_{12}$

$Li_{6.5}Sm_3Sn_{1.5}Ta_{0.5}O_{12}$

$Li_7Nd_3Sn_2O_{12}$

$Li_{6.5}Sm_3Zr_{1.5}Ta_{0.5}O_{12}$

$Li_7Pr_3Zr_2O_{12}$

$Li_{6.5}Nd_3Zr_{1.5}Ta_{0.5}O_{12}$

Ceramics with high sintering temperatures

α-Al_2O_3 was sintered from Al_2O_3 (99.9%, Sigma Aldrich).

Y-stabilized ZrO_2 (YSZ) was sintered with a composition of 8% Y_2O_3 and 92% ZrO_2 (99.9%, Sigma Aldrich).

Non-garnet-based solid-state electrolytes

LATP was sintered with a composition of $Li_{1.3}Al_{0.3}Ti_{1.7}(PO_4)_3$ from stoichiometrically mixed raw materials of Li_2CO_3, Al_2O_3, $NH_4H_2PO_4$, and TiO_2 (99.9%, Sigma Aldrich). The precursors were pre-sintered at 500 ℃ for 30 mins to decompose $NH_4H_2PO_4$.

LLTO was sintered with the chemical formula of $Li_{0.3}La_{0.567}TiO_3$ from stoichiometrically mixed raw materials of Li_2CO_3 (99.9%, Sigma Aldrich), La_2O_3 (≥ 99.9%, Sigma Aldrich), and TiO_2 (99.9%, Sigma Aldrich).

Mixed ionic-electric conductor

LLMO was sintered with the chemical formula of $Li_7La_3Mo_2O_{12}$ from stoichiometrically mixed raw materials of Li_2CO_3 (99.9%, Sigma Aldrich), La_2O_3 (≥ 99.9%, Sigma Aldrich), and MoO_2 (99.9%, Sigma Aldrich), with 10% excess Li.

Preparation of the co-sintered all solid-state batteries

To assemble the co-sintered all solid-state batteries, the LLMO precursors were coated on the UHS-sintered LLZTO garnet pellet for UHS sintering. Then a thin layer (~2 μm) of carbon nanotubes (P3-CNTs, Carbon Solution) was coated on the sintered LLMO electrode to act as the current collector. Li metal was coated on the other side of the LLZTO pellet to act as the anode.

Materials characterization

The morphologies and elemental mapping of the samples were conducted by scanning electron microscopy (SEM; Hitachi SU-70) coupled with an energy dispersive X-ray spectroscopy (EDS)

detector at 10 kV. X-ray diffraction (XRD) measurements were performed on a C2 Discover diffractometer (Bruker AXS, WI, USA) using a Cu Kα radiation source operated at a voltage of 40 kV and a current of 40 mA. The Li contents of the UHS and conventional furnace sintered LLZTO garnet samples were analyzed by inductively coupled plasma mass spectroscopy (PerkinElmer NexION 300D ICP-MS). The solutions were prepared by digesting the samples in aqua regia followed by diluting with 18 MΩ pure water.

Electrochemical measurements

Electrochemical tests of the Li/garnet/Li symmetric cells were conducted on a BioLogic VMP3 potentiostat at room temperature. Li was coated on the garnet surface using molten Li with ~30 wt% Sn at ~250 ℃. Electrochemical impedance spectroscopy (EIS) was performed with 20 mV AC amplitude in the frequency range of 100 mHz to 1 MHz for the Li/garnet/Li cells. Galvanostatic stripping-plating of the Li/garnet/Li symmetric cells was recorded at room temperature with different current densities. The cells were placed in an argon-filled glovebox to conduct all electrochemical measurements at room temperature.

Neutron depth profiling (NDP) measurements

The *in situ* NDP measurements were conducted at the National Institute of Standards and Technology (NIST) Center for Neutron Research at the NG1 Cold Neutron Depth Profiling station following a previous method (*28*). A ~2-5 μm layer of Li metal was coated on the garnet surface for better signal in the NDP measurement. The cells for NDP were measured in an ultra-high vacuum chamber at room temperature.

Simulations of temperature distribution in sample pellet during UHS process

The temperature distribution of the sample during heating was investigated using a numeric model. This numeric model was created based on the commercial finite element software ANSYS. A

linear temperature increases from room temperature (22 ℃) to 2,000 ℃ in 10 s (or 30 s) followed by a constant temperature of 2,000 ℃ for 10 s was imposed as a boundary condition on the sample/Argon caused by the Joule heating of the carbon heaters. Geometry parameters used in this numeric model are listed in Table S1 unless otherwise noted.

Table S1. Geometry Parameters Used in the Numeric Model

Model Component	Shape	Dimensions
LLZTO pellet	cylinder	Diameter = 10 mm, Thickness = 1 mm
Carbon Heater	Square prism	20 mm x 20 mm x 1 mm

Thermal properties of the LLZTO pellet used in this numeric model were measured, which were listed in Table S2 unless otherwise noted. The heat capacity of the LLZTO pellet was measured using DSC Q100 from TA instrument, and the thermal conductivity was measured using a steady-state method(*35*). The IR transmittance of the LLZTO green pellets with different thickness was measured using a Thermo Nicolet NEXUS 670 FTIR, which can be used to determine the absorbance and reflectance of the pellet samples. All these measurements were conducted at room temperature. These properties were assumed to be temperature-independent in the numeric model.

Table S2. Material properties Used in the Numeric Model

Materials	Specific heat capacity (J/g/K)	Thermal conductivity (W/m/K)	Density (g/cm^3)	Absorbance	Reflectance
LLZTO (Before sintering)	0.385	0.18	2.5	0.25	0.72
LLZTO (After sintering)	0.242	1.29	5		
Argon Gas	0.521	Ref.(*36*)	Ideal gas law	0	0

The properties of the LLZTO pellets changed during the sintering process, as evidenced in Table S2. In this numeric model, six cases were employed to investigate the temperature distribution

during the sintering process:

Case A1: Thermal properties of the LLZTO pellet before sintered were used. The absorbance of the pellet was assumed to be zero. The gap between top surface of the pellet and the carbon heater was set to be 0.25 mm. The heating ramping time is 10 s.

Case A2: Thermal properties of the LLZTO pellet after sintered were used. The absorbance of the pellet was assumed to be zero. The gap between top surface of the pellet and the carbon heater was set to be 0.25 mm. The heating ramping time is 10 s.

Case A3: Thermal properties of the LLZTO pellet before sintered were used. The absorbance of the pellet was assumed to be zero. The gap between top surface of the pellet and the carbon heater was set to be 0.25 mm. The heating ramping time is 30 s.

Case A4: Thermal properties of the LLZTO pellet before sintered were used. The absorbance of the pellet was assumed to be 0.25. The gap between top surface of the pellet and the carbon heater was set to be 0.25 mm. The heating ramping time is 30 s.

Case A5: Thermal properties of the LLZTO pellet before sintered were used. The absorbance of the pellet was assumed to be 0.25. The gap between top surface of the pellet and the carbon heater was set to be 0 (i.e., no gap). The heating ramping time is 30 s.

Case A6: Thermal properties of the LLZTO pellet after sintered were used. The absorbance of the pellet as assumed to be 0.25. The gap between top surface of the pellet and the carbon heater was set to be 0.25 mm. The heating ramping time is 30 s.

Figure S1(A) shows the temperature contours of the LLZTO pellet for the six simulation cases mentioned above. The temperature contours were taken after the heating ramping but before the 10 seconds holding. Figure S1(B) shows the difference between the maximum and minimum temperature within LLZTO pellet as a function of the heating time for the six simulation cases

(A1-A6). As seen in this figure, a lower heating rate (e.g., 30 s ramping) results in a more uniform temperature distribution in the LLZTO pellet. The 30 s ramping time was used in the UHS process in our experiment. The temperature difference within the LLZTO pellet is generally less than 100 ℃ during the heating ramping process, as suggested by the numeric simulation. In all six simulation cases, the temperature difference rapidly decreases to nearly zero during 10 s holding stage for all cases.

First-principles calculations

All density functional theory (DFT) calculations were performed using the projector augmented-wave (PAW) (*37*) approach with the Perdew-Burke-Ernzehof (PBE) generalized gradient approximation (GGA) (*38*) implemented in the Vienna *Ab initio* Simulation Package (VASP) (*39*). All parameters used in the calculations were consistent with the Materials Project (*40*) to achieve energy convergence of 1 meV per atom. The phase equilibria of the materials were calculated by constructing the phase diagram using the *pymatgen* code (*41*), according to previous studies (*30*, *42*). The voltage profile of $Li_xLa_3Mo_2O_{12}$ (LLMO) was calculated by identifying stable phases at Li intermediate concentrations. We adopted a Hubbard potential (*43*) as 4.38 V on the *d* states of Mo from the Materials Project to calculate the voltage profile accurately (*40*).

We employed the computational workflow to explore a new set of $Li_7A_3B_2O_{12}$ garnet materials. While the most exhaustive sampling of all 89 elements as potential cations in candidate $Li_7A_3B_2O_{12}$ compounds would yield over 7000 compositions, it is computationally expensive to compute all those structures. Since stable materials should satisfy the Pauling's rule (*44*), we were able to narrow down the list of candidate compounds by selecting those that satisfy the charge balance and the Pauling's radius ratio rule. To satisfy the criteria of the radius ratio, A-site cations coordinated with eight O^{2-} or the B-site cation with six-fold coordination should be larger than

0.81 or 0.52 Å, respectively, with a radius of O^{2-} as 1.26 Å using the Shannon crystal ionic radius (*45*). We then evaluated the phase stabilities of those selected compounds by calculating the energy above the hull, using the established method in *pymatgen*, as in previous studies (*26*).

Material synthesis and fabrication of the 3D-printed SiOC structures

All chemicals were purchased from either Sigma-Aldrich or Gelest and were used as received. Genocure TPO-L liquid initiator for the UV curing process was generously donated by Rahn AG. To synthesize Co-doped magnetic SiOC resins, 28.3 g of 3-(trimethoxysilyl)propyl methacrylate (TMSPM), 6 g of ethanol, 0.975 g of acrylic acid, and 3.3 g of cobalt nitrate hexahydrate were combined. Separately, we mixed 2 g of deionized water and 0.08 g of concentrated hydrochloric acid. Then we added this solution dropwise to the TMSPM mixture under vigorous stirring, followed by heating at 100 °C for 2 h. After heating, 0.56 g (2wt% to TMSPM) of phenylbis(2,4,6-trimethylbenzoyl)phosphine oxide and 0.014 g (0.05 wt% to TMSPM) Sudan I dye were added and dissolved by gentle heating and mixing. To synthesize Al-doped SiOC resins, we used a formula based on the work of Cui et al. (*46*). 10 g of Gelest SMS-992, (mercaptopropyl)methylsiloxane homopolymer, was combined with TMSPM, aluminum-tri-sec-butoxide, and 0.2% Sudan I. The solution was then mixed with Gelest VMM-010, vinylmethylsiloxane homopolymer, and TPO-L.

These resins (Co-doped and Al-doped SiOC) were 3D printed using a custom-made multi-material stereolithography system similar to the work reported by Chen et al. (*47*). A fluidic system deposits the Co-doped SiOC resin onto a transparent membrane. The printing stage moves down towards the transparent membrane and leaves a specific distance (equal to the layer thickness) to the membrane. A programmed light pattern based on the sliced CAD model illuminates the resin and generates a solid only in the light-exposed areas. The build platform elevates and can either

be replenished with new Co-doped SiOC resin to build further layers or be cleaned with automated ethanol and air, and then dipped into the Al-doped SiOC, which is similarly exposed to light, binding it to previous layers. In this way the two materials are combined in specified areas.

Calibration of the magnetic flux density sensor

The resistance change (ΔR) of the piezoresistive material is described by the following relationship: (*48*)

$$\Delta R = \frac{G_s \sigma}{E_s} R \qquad (S1)$$

in which G_s is the gauge factor of the piezoresistive material, σ is the applied stress, E_s is the Young's modulus of the material, and R is the original resistance of the material without the applied stress.

For the as-fabricated honeycomb piezoresistive structure (Al-doped SiOC), equation S1 can be written as,

$$\Delta R = \frac{G_h \sigma}{E_h} R \qquad (S2)$$

in which G_h is the gauge factor of the as-fabricated honeycomb structure, which stays constant within the small stress range presented in this study, while E_h is the out-of-plane Young's modulus of the honeycomb structure and was 500 MPa and 303 MPa for the samples sintered by the UHS method and the conventional sintering method, respectively. The testing was performed on an INSTRON 5944 by compression with a strain rate of 0.001/s.

Fig. 4H shows the resistance change of the Al-doped SiOC sintered by the UHS method and the conventional method as a function of applied stress induced by the Co-doped SiOC component under a magnetic field. By substituting the resistance change, stress change, and E_h of the

honeycomb structure into Eq. S2, the gauge factors of the piezoresistive section of the sensors sintered by the UHS and conventional sintering methods were calculated to be 297 and 137 (Fig. S36C), respectively.

The stress applied on the piezoresistive honeycomb structure under a magnetic field (σ_m) can be calculated by: (*49*)

$$\sigma_m = \frac{0.5\chi V B^2}{u_0 h A} \qquad (S3)$$

in which χ is the susceptibility of the magnetic material (Co-doped SiOC), V is the volume of the magnetic material, B is the magnetic flux density, u_0 is the permeability of a vacuum, h is the height of the magnetic material, and A is the cross-sectional area of the piezoresistive material (Al-doped SiOC).

Here we define $K_m = \frac{0.5\chi V}{u_0 h A}$ as the magnetic field sensitivity of the magnetic section of our sensor and Eq. (S3) becomes

$$\sigma_m = K_m B^2 \qquad (S4)$$

Fig. S31B shows the stress applied on the Al-doped SiOC as a function of the magnetic flux density. The magnetic field sensitivity is calculated based on the fitted curve, as shown in Fig. S29B.

By combining Eqs. S4 and S2, we can obtain the resistance change of the Co- and Al-doped SiOC multi-material specimen (Fig. S31D) as a function of the applied magnetic flux density.

$$\Delta R = \frac{G_h K_m R}{E_h} B^2 \qquad (S5)$$

Here we define $K = \frac{G_h K_m R}{E_h}$ as the sensitivity of our magnetic flux density sensor, in which K equals 500 Ω/T^2 and 380 Ω/T^2 at 25 °C and 200 °C, respectively.

After sintering the multi-material honeycomb structure by the UHS technique (~1,200 ºC, 10 s), two copper leads were attached onto the piezoresistive section of the polymer-derived ceramic using a conductive silver paint (Leitsilber 200 Silver Paint) (Fig. S31A). A permanent magnet was used to generate various magnetic fields (quantified with SJ200 TESLAMETER) by varying the distance to the as-fabricated sensor. A digital multimeter (MASTECH MY64) was then used to read the resistance of the piezoresistive section of the sensor through the copper leads, after which the resistance change and magnetic field was correlated, as shown in Fig. S31D.

Supporting Figures

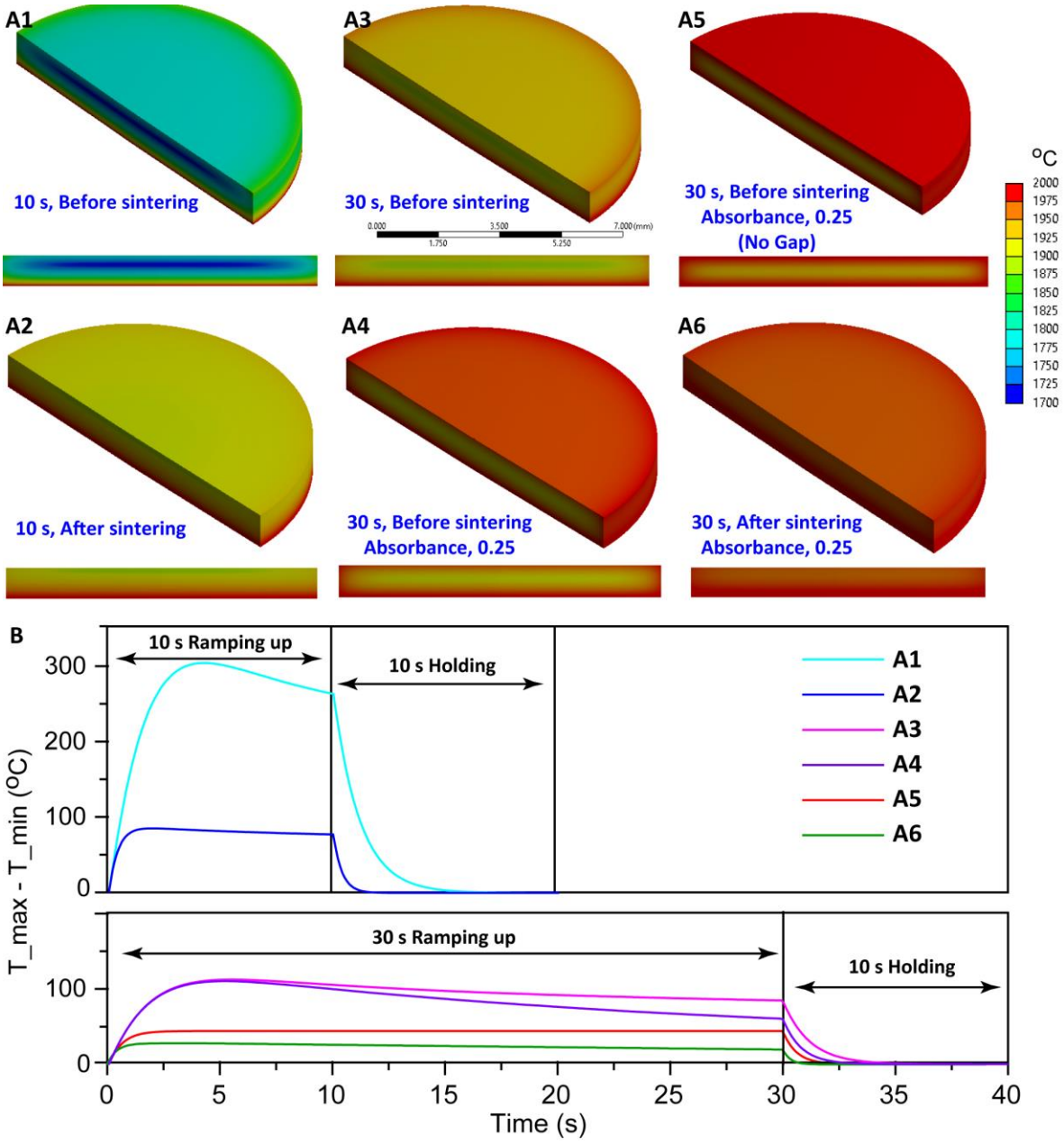

Figure S1: Temperature contours of the LLZTO pellet for the six simulation cases (A1-A6) The temperature contours were taken after the heating ramping but before the 10 s holding. (B) The difference between the maximum and minimum temperature within LLZTO pellet as a function of the heating time for the six simulation cases (A1-A6). The temperature difference rapidly decreases to nearly zero during 10 s holding stage for all cases.

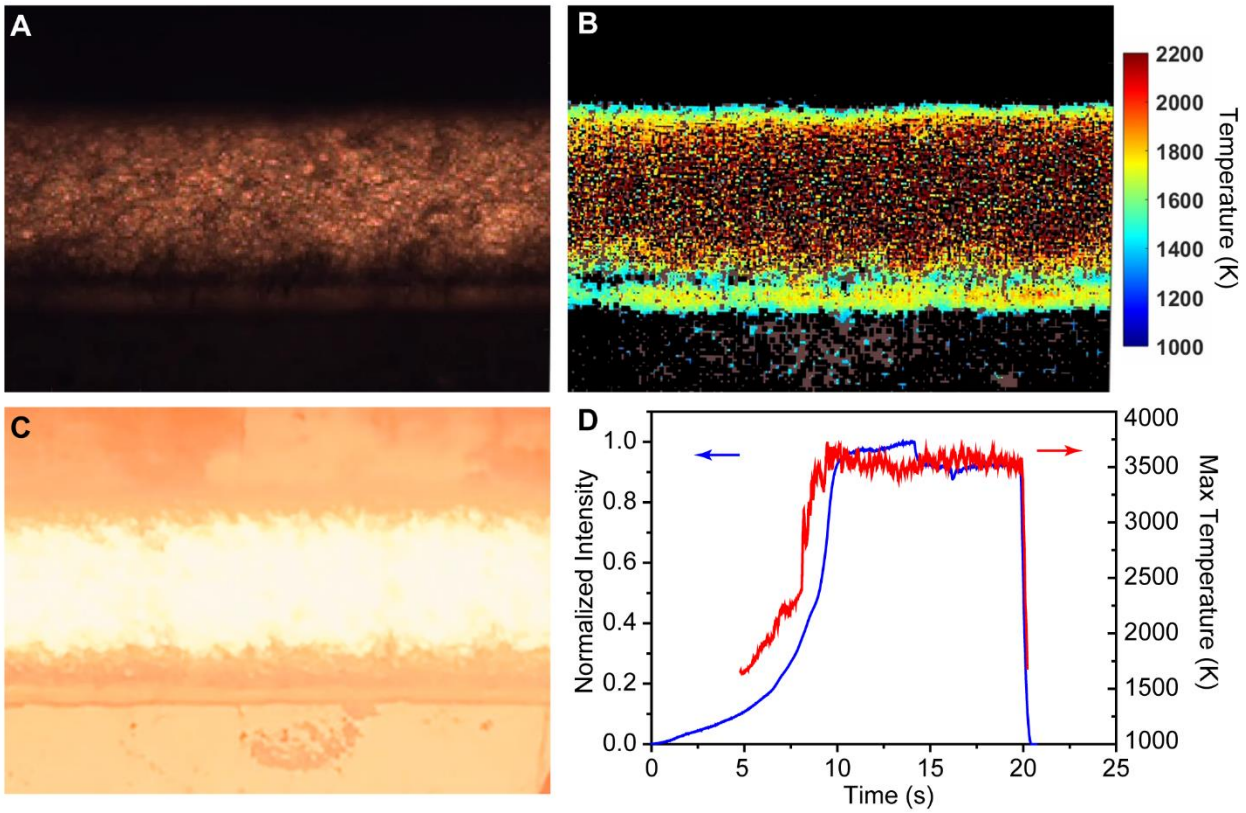

Figure S2. UV-Vis spectrum of the UHS carbon heaters for temperature measurement. (A) Photograph and (B) the corresponding temperature distribution of the UHS carbon heating elements captured with a UV-Vis camera. (C) Typical photograph of the heaters at ~3,000 ^{o}C. (D) The normalized light intensity and maximum temperature curves of the heating element derived from the UV-Vis camera. The UV-Vis measurements demonstrate that the high temperature can reach up to 3,000 ℃ in ~10 s, followed by a fast cooling rate of ~ 10^4 ℃/min.

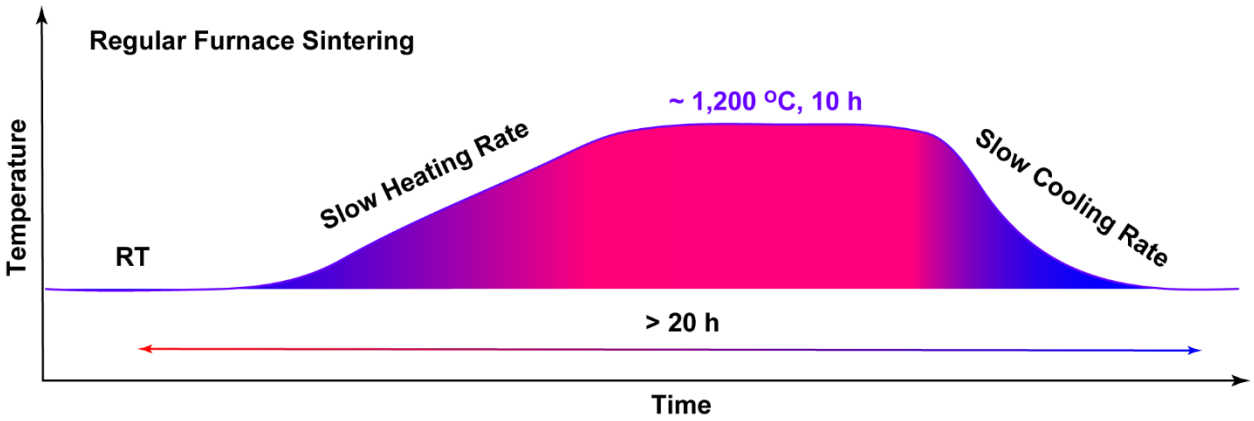

Figure S3. Typical temperature profile of conventional furnace sintering techniques. The slow heating (3-10 ℃/min) and cooling rates (3-5 ℃/min) and long sintering time (~10 h) make the whole process take more than 20 h. In sharp contrast, the sintering time of the UHS technique is only ~10 s, which is more than 3,000-times faster.

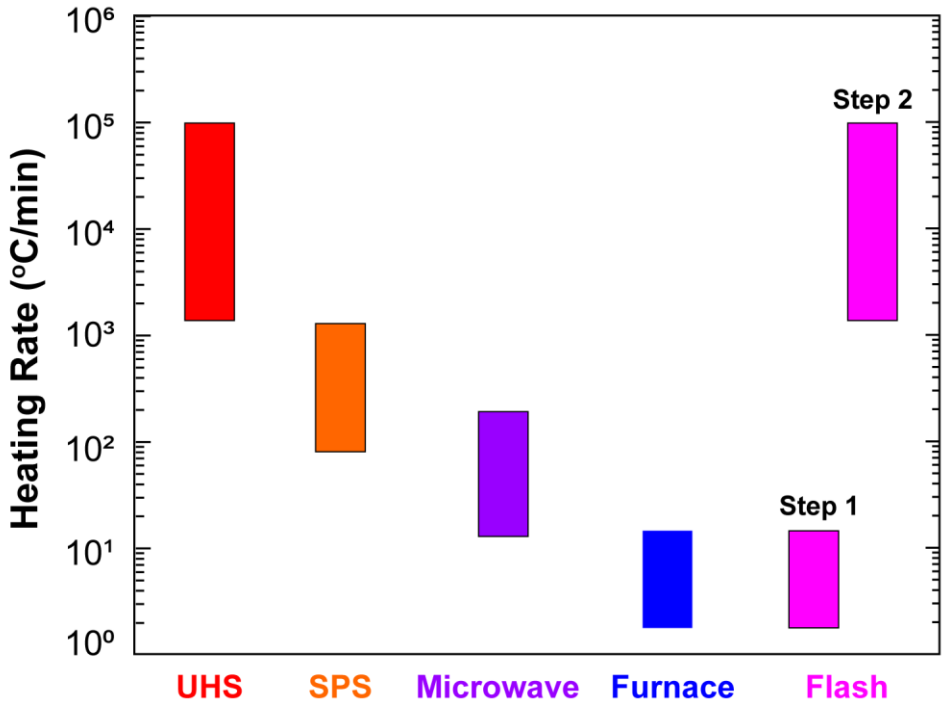

Figure S4. Comparison of different sintering methods. The UHS technique has a higher heating rate than regular furnace, spark plasma sintering (SPS), and microwave-assisted sintering. Flash sintering has a comparable flash heating rate to UHS, but normally requires preheating using a regular furnace, which has a low heating rate.

Table S3. Typical parameters of different rapid sintering methods. Comparing the key parameters of the rapid sintering methods, the UHS technique has a much higher heating rate (~10^3–10^4 ℃/min) and cooling rate (up to 10^4 ℃/min), requires much less sintering time (1–10 s), can reach a temperature of up to 3,000 ℃, and features minimal sample requirements, making it a general sintering method. The ultrafast sintering process of the UHS technique enables the realization of complex ceramic structures and co-sintering of multilayer structures.

	Microwave	**SPS**	**Flash sintering**	**UHS**
Max Temperature (℃)	Typically up to ~2,000	up to 2,500	Currently limited by the T_{melt} of the Pt electrodes	up to 3,000
Sintering time (s)	Typically ~600	200–1,000	5–30	Typically 1–10
Heating rate (℃/min)	10–10^2	10^2–10^3	Two steps: ~10 (Preheating); ~10^3–10^4 (Flashing Stage)	~10^3–10^4 (Controllable)
Mechanical Compression	Not needed	Needed	Not needed	Not needed
3D printed structures or membranes	Can maintain structure	Hard to maintain structure	Hard to maintain structure	Easy to maintain structure
Batch processing	Different composition	Different compositions	One composition	Different compositions
Sample requirements	Not Materials Specific with Susceptor	Not Materials Specific	Materials Specific (depending on electric properties)	Not Materials Specific

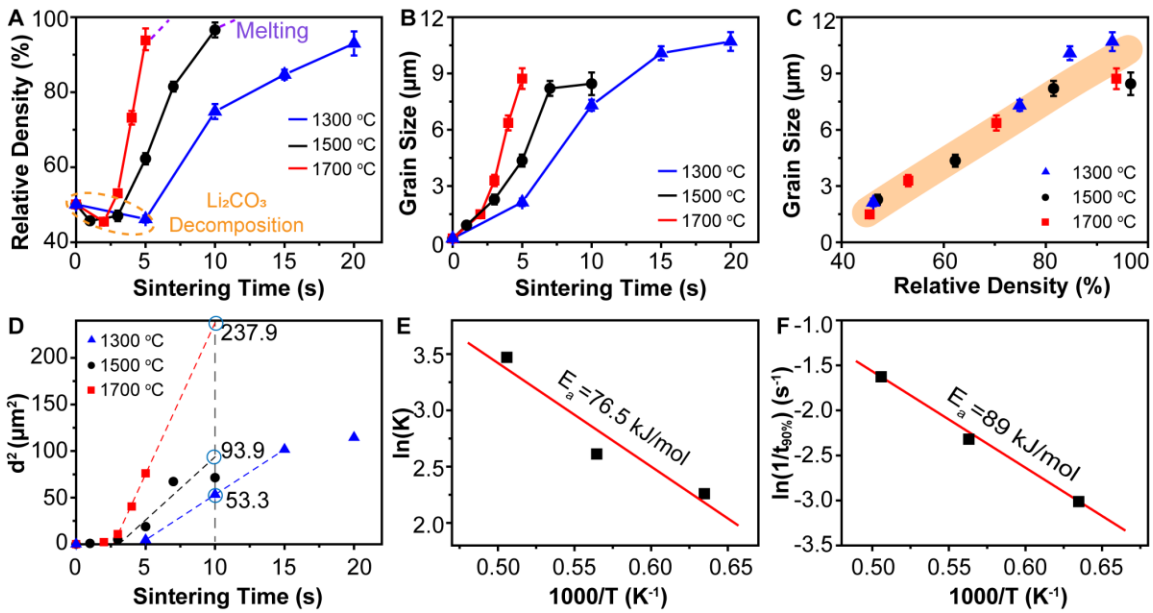

Figure S5. Relationship of relative density and grain size with sintering time for LLZTO at three different isothermal holding temperatures. (A) Relative density as a function of sintering time at three different isothermal holding temperatures (on the surface as measured by pyrometry). The initial drop in the relative density is attributed to continuing reaction (possibly the final stage of decomposition of lithium carbonate). At the isothermal holding temperatures of 1,500 °C and 1,700 °C, the specimens partially melted for long holdings; the delays in partial melting could be caused by times needed for the heat transfer and/or the phase transformation kinetics. (B) Grain size as a function of sintering time at different sintering temperatures. (C) Relationship between grain size and relative density at different sintering temperatures, which show similar trends at three different temperatures. (D) Squared grain size vs. sintering time curve, which show a classical parabolic grain growth in the intermediate sintering stage. The linear parts are used to fit the slope *K* for estimating the activation energy of grain growth in (E) via an Arrhenius plot of ln(K) vs. 1000/T. (F) The Arrhenius fitting of the time of achieving 90% relative density ($t_{90\%}$) as a function of sintering temperatures, plotted in $\ln(1/t_{90\%})$ vs. 1000/T for estimating an activation energy.

Based on the thermally etched SEM images, we systematically studied the variation of the average grain size and relative density with different sintering conditions (Fig. S5), which provide a deeper understanding of the sintering mechanism of the UHS technique. Fig. S5A plots the relative density as a function of sintering time at three different isothermal holding temperatures. The initial drop in the relative density is attributed to continuing reaction, mostly likely the final stage of the decomposition of lithium carbonate. Specifically, the green garnet pellets complete the densification process within ~5-20 s at a sintering temperature of ~1,300 ℃. At higher sintering temperatures of ~1,500 ℃ and ~1,700 ℃, the densification times decrease to 10 s and 5 s, respectively. At the isothermal holding temperatures of ~1,500 °C and ~1,700 °C, the specimens partially melted for long holdings; the delays in partial melting could be caused by times needed for the heat transfer and/or the phase transformation kinetics, which also have time scales of seconds. In this regard, the ultrafast sintering here is not a near-equilibrium process. Similar to the relative density trend, the grain grows faster with higher sintering temperatures (Fig. S5B). However, the final grain size is about 8-10 μm, which are similar for three different isothermal temperatures, with different durations to achieve similar final densities.

Interestingly, the three grain size *vs.* relative density curves at different sintering temperatures largely overlap regardless the isothermal holding temperatures (Fig. S5C), which indicates a similar grain growth and densification mechanisms for UHS in a wide temperature range. In comparison with conventional sintering, the grain size increases almost linearly with the relative density, where a final-stage rapid grain growth is not observed.

The following grain growth equation was used to analyze the grain growth mechanism:

$$d^n - d_0^n = K \cdot t$$

where d is the average grain size at annealing time t, d_0 is the initial grain size, n is the grain growth

exponent. Here, the grain growth kinetic constant:

$$K = k_0 \cdot exp(E_a/RT)$$

where k_0 is a constant, E_a is an activation energy, R is the gas constant, and T is the absolute temperature. For the grain growth exponent, n, it typically equals to 2 or 3.

To have a direct comparison with the results of other LLZO garnets, we choose n = 2, same value reported in Sakamoto's work (*20*) for the analysis. On the d^2 *vs t* plot (Fig. S5D), the linear parts in the intermediate sintering stage of each curve associating with the rapid grain growth were used to fit the slope K for estimating the activation energy of grain growth. From the plot in Fig. S5E, the activation energy was calculated to about 76.5 kJ/mol, which is much lower than the value of 560 kJ/mol reported Sakamoto's work (*20*).

The time of achieving 90% relative density (t90%) at different sintering temperatures was also used as to estimate activation energy by an Arrhenius fitting of ln(1/t90%) vs. 1/RT (Fig. S5F), which produces a similar activation energy of 89 kJ/mol.

The lower activation energies suggested that sintering and grain growth mechanisms in UHS process are somewhat different with those in conventional sintering. We attributed the differences to the fact that the ultrafast sintering here is not a near-equilibrium process, which is also suggested by the grain growth vs. relative density curves. First, the heat transfer, phase transformation (e.g., partial melting at high sintering temperatures of 1,500 ℃ and 1,700 ℃ for LLTZO shown here) are have comparable time scales with the densification and grain growth in UHS in seconds (vs. densification and grain growth rates are lower in conventional sintering at longer time). It is possible that nonequilibrium (not relaxed) grain boundaries can form with the ultra-fast heating rate and high sintering temperatures (*15*, *19*). In-depth mechanisms will be investigated in a future study.

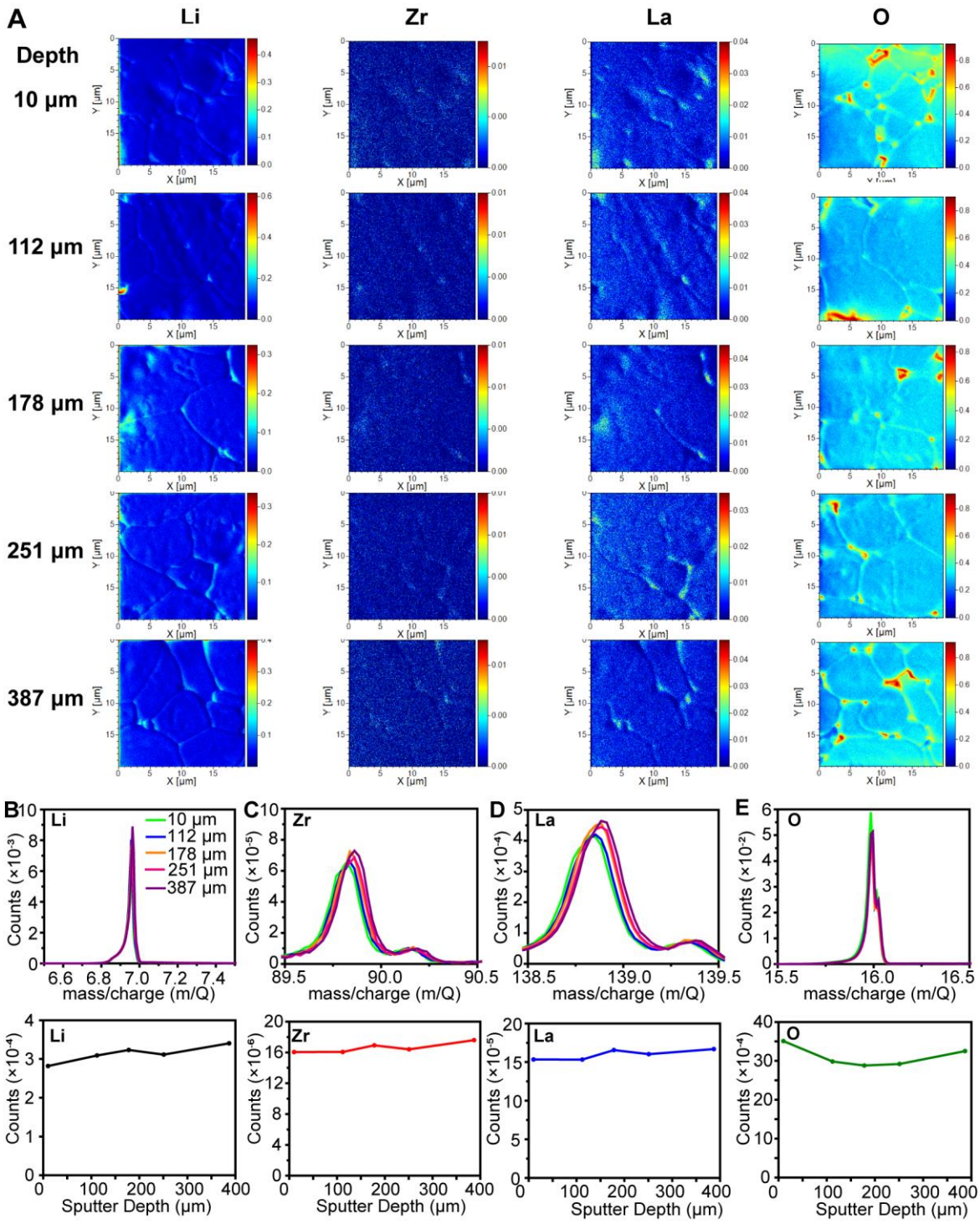

Figure S6. (A)TOF-SIMS mapping of Li, La, Zr, and O elements at different depths across the thickness of the sintered garnet pellet from one surface to the other surface. The Li, La, Zr, and O elements are uniformly distributed through the bulk of the sintered garnet pellet with no

obvious deficiency or aggregation phenomenon. TOF-SIMS spectra (top) and the corresponding integrated counts (bottom) for (B) Li, (C) Zr, (D) La, and (E) O elements at different depths across the thickness of the sintered garnet pellet from one surface to the other surface. The uniform element distribution through the cross-section of the sintered garnet pellet demonstrates the unique superiority of the UHS technique at inhibiting the vaporization of volatile elements and maintaining the stoichiometry.

To characterize the element distribution as a function of distance from the sample surface, we conducted Time of Flight Secondary Ion Mass Spectroscopy (TOF-SIMS) measurements. As Figure S6A shows, the main elements, including the most volatile element (Li), in LLZTO garnet have relatively uniform distribution as a function of distance from the sample surface. More quantitative analysis in Figure S6B-E also indicates negligible variation. The slight difference in Oxygen is mainly due to the accumulation of some secondary phases at the grain boundaries, which could be lithium carbonate formed in air during sample transport.

Therefore, the sintered LLZTO pellet has uniform elemental distribution, and we observed no surface deficiency of volatile element. Though evaporation from a surface is a thermally activated process, we ascribe the absence of any volatile element deficiency to the ultrafast sintering process of the UHS technique. Additionally, the internal Li from the sample bulk can potentially compensate any slight surface evaporation due the fast diffusion rate of Li at high temperature, which leads to uniform Li distribution in the sintered pellets.

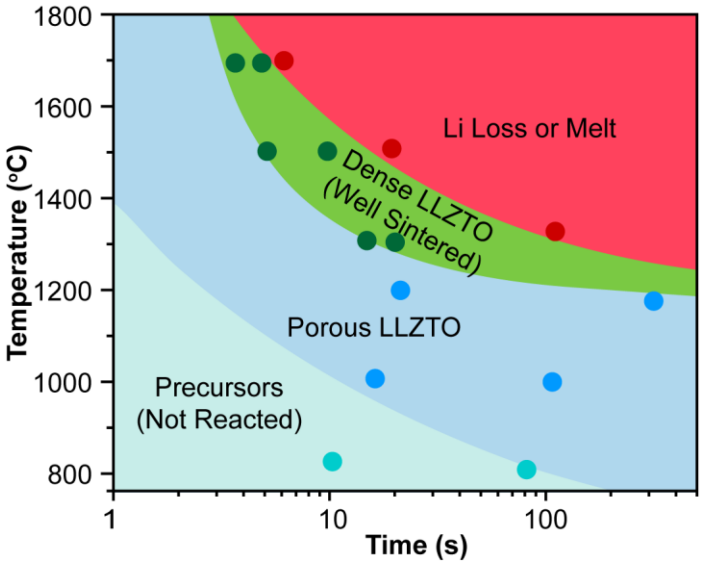

Figure S7. Schematic Time-Temperature-Transformation diagram of LLZTO garnet based on Raman and XRD results, illustrating the evolution of the LLZTO garnet during the UHS process.

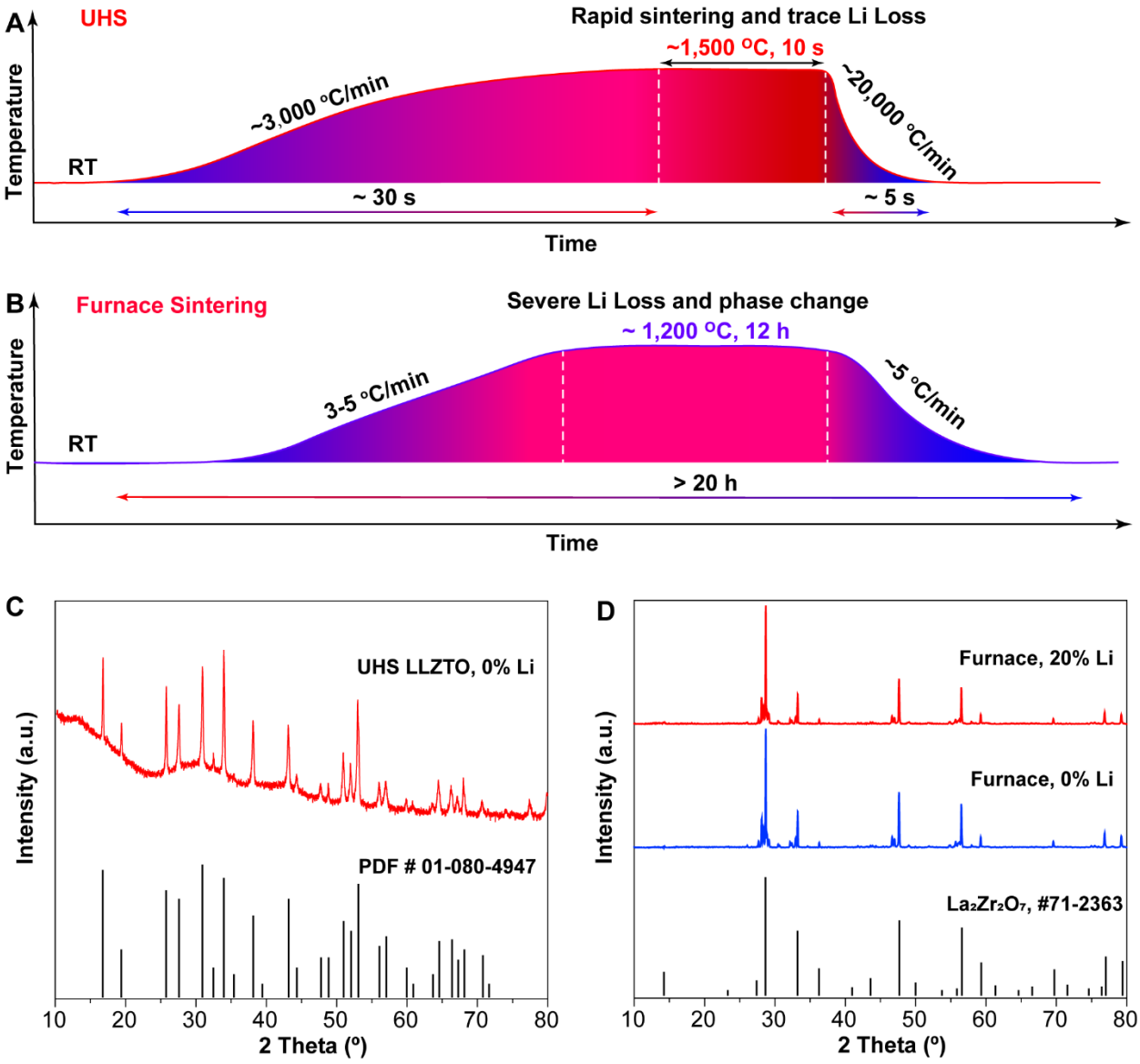

Figure S8. Comparison of UHS and regular sintering of LLZTO garnet materials. Typical temperature profiles of (A) the UHS and (B) conventional furnace synthesis of the LLZTO garnet. XRD patterns of (C) the UHS-sintered and (D) conventional-furnace-sintered LLZTO garnet samples with different excess Li contents. The garnet sintered by UHS exhibits the pure cubic garnet phase, even when using 0% excess Li. However, the LLZTO garnet samples sintered in the conventional furnace feature a pure $La_2Zr_2O_7$ structure, indicating severe Li loss, even for the

sample made with 20% excess Li. The precursors with different excess Li compensation were sintered in a conventional furnace at 1,200 ℃ for 10 h. The ultrafast sintering process of UHS (~1,500 ℃, ~10 s) makes the total fabrication time of the LLZTO garnet less than 50 s, which is much shorter than the conventional sintering method (~22 h). Additionally, there is no need to compensate for Li loss during UHS sintering.

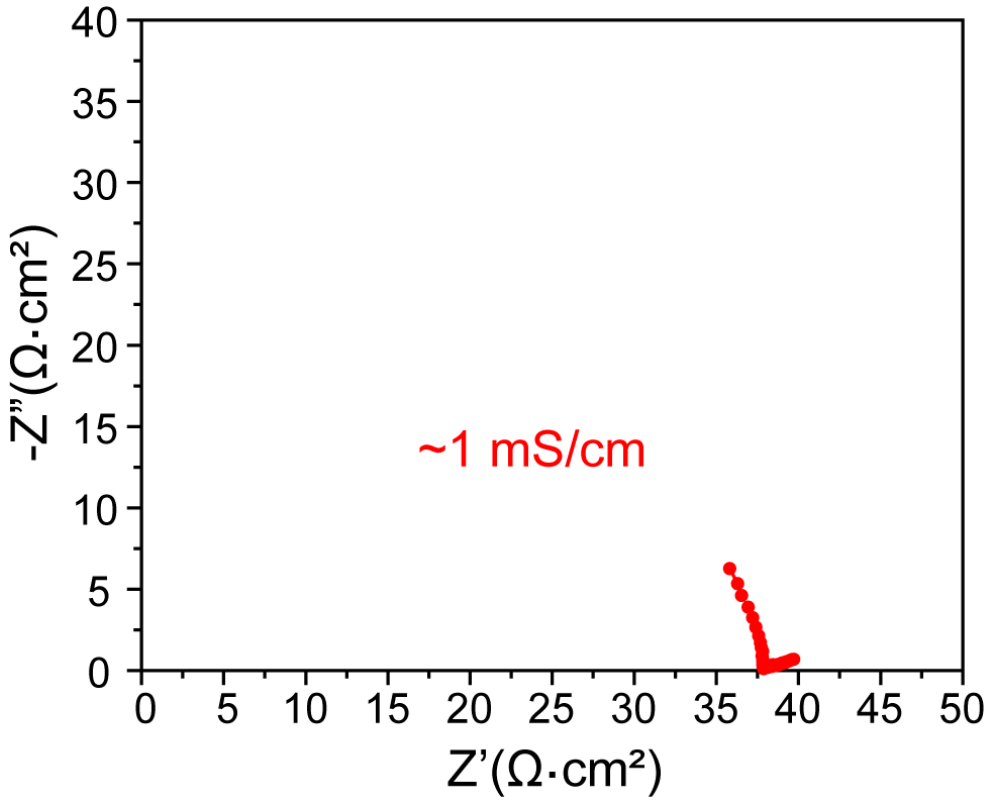

Figure S9. Typical EIS measurement of the UHS-sintered garnet SSE, made with a sintering temperature of 1,500 ℃ for 10 s. The ionic conductivity was calculated to be ~1 mS/cm, among the highest reported in the literature.(*18*, *23*)

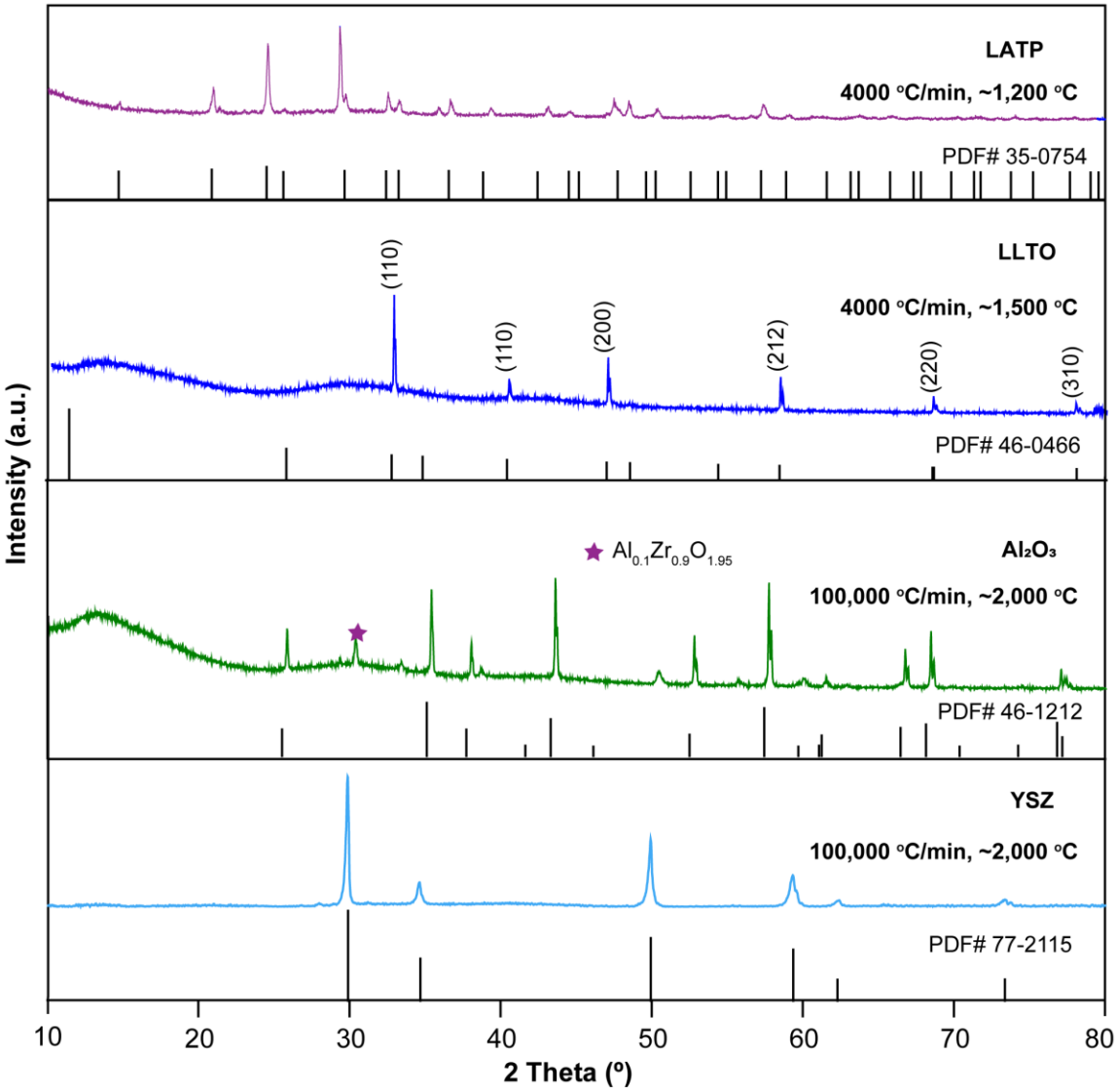

Figure S10. XRD Patterns of the LATP ($Li_{1.3}Al_{0.3}Ti_{1.7}(PO_4)_3$), LLTO ($Li_{0.3}La_{0.567}TiO_3$), Al_2O_3, and YSZ made by UHS sintering. The XRD results demonstrate that LATP, LLTO, and YSZ were successfully synthesized by the UHS technique from precursors in a single step, with no phase impurities. Al_2O_3 exhibits the α-Al_2O_3 structure with little secondary phase of $Al_{0.1}Zr_{0.9}O_{1.95}$, which is due to the slight ZrO_2 doping that occurs during the 6 h ball-milling process, which utilizes a ZrO_2 milling jar and balls. Therefore, the UHS technique can be applied for the rapid synthesis of a wide range of ceramic materials.

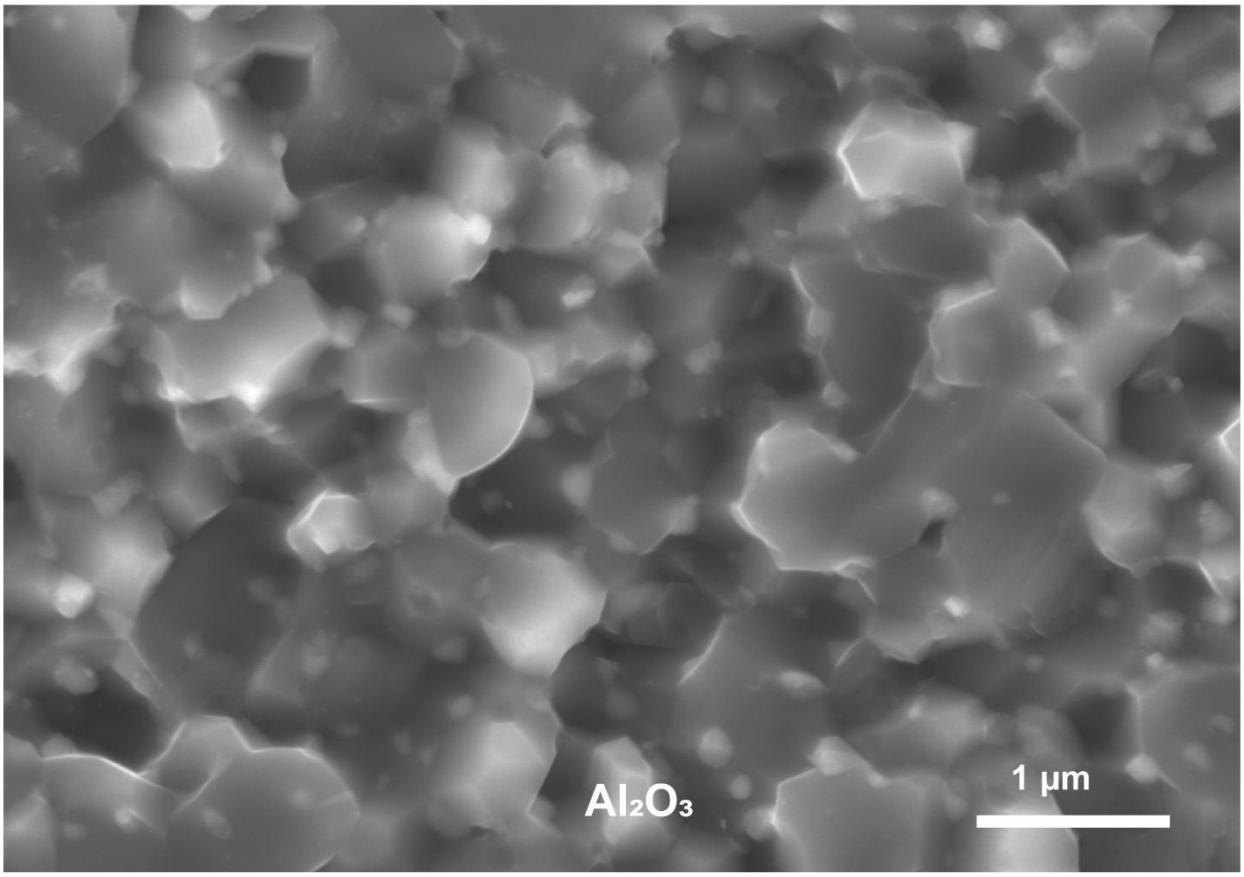

Figure S11. SEM image of the UHS-sintered Al_2O_3 pellet. The Al_2O_3 pellet sintered at ~2,000 ℃ for ~10 s features a dense morphology and tightly bonded grains, with relative densities above 96%.

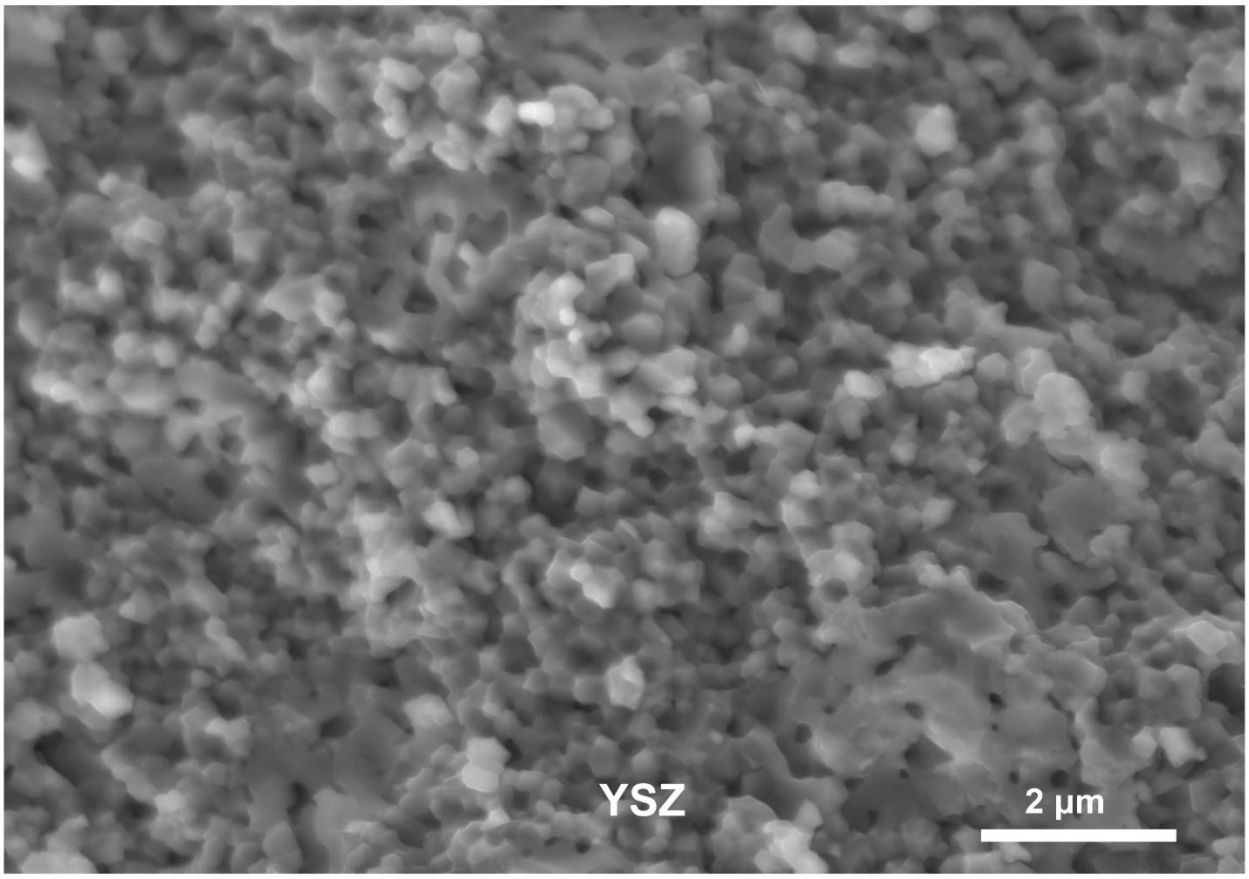

Figure S12. SEM image of the UHS-sintered Yttria-stabilized ZrO_2 (YSZ). The nanoscale grains are uniform and tightly bonded, with relative densities above 95%.

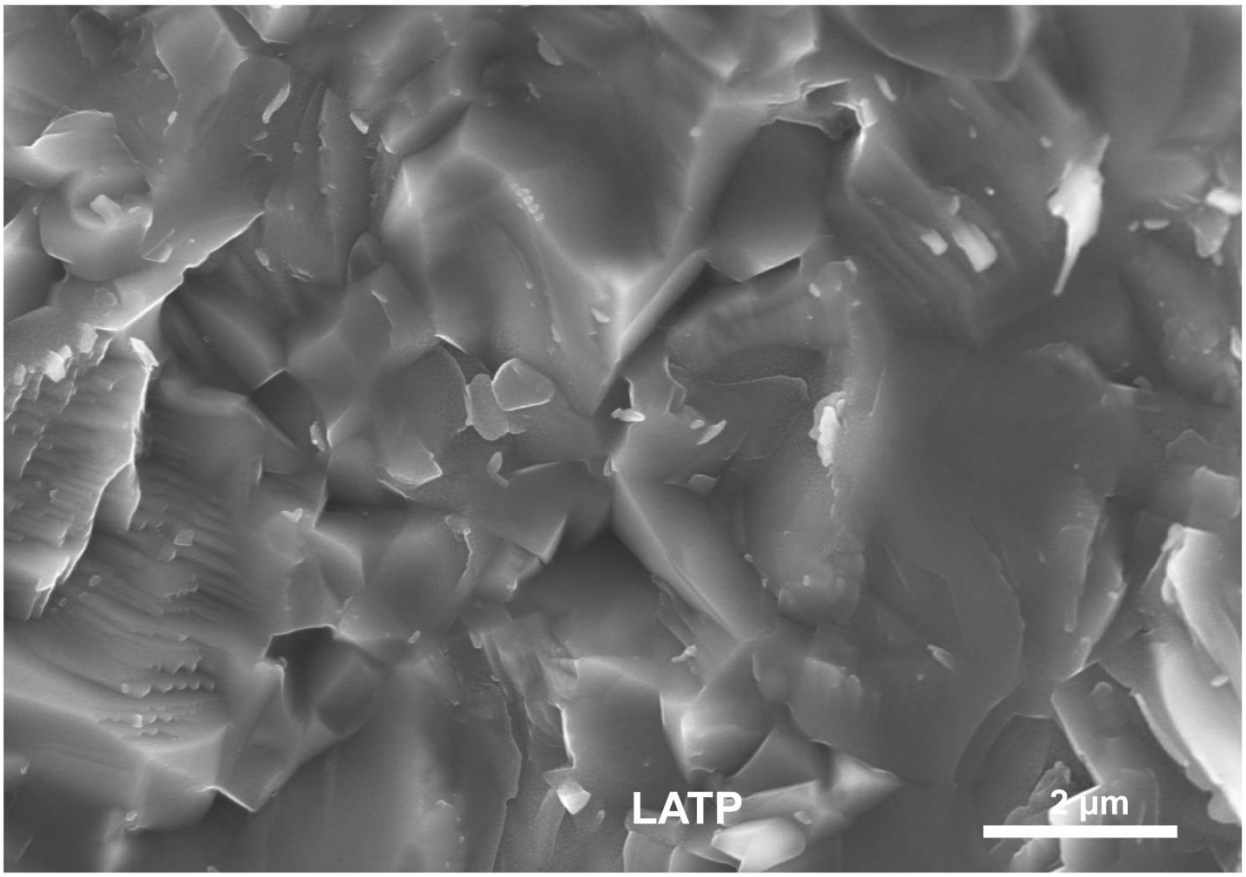

Figure S13. SEM image of the UHS-sintered $Li_{1.3}Al_{0.3}Ti_{1.7}(PO_4)_3$ (LATP). The sample shows a dense morphology with well-merged grains, with relative densities above 90%.

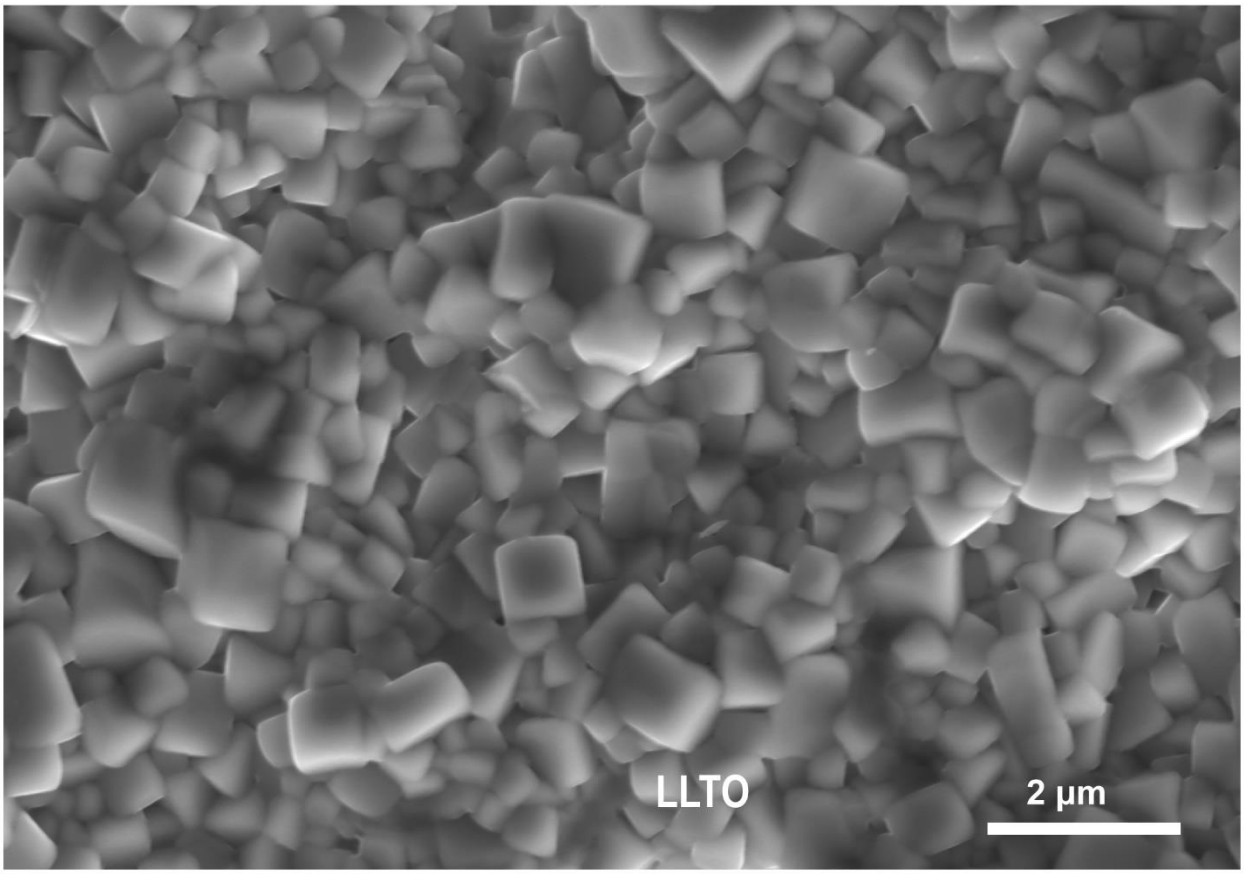

Figure S14. SEM image of the UHS-sintered $Li_{0.3}La_{0.567}TiO_3$ (LLTO). The sample pellet features uniform nanoscale grains and tightly-bonded grain boundaries, with relative densities above 94% due to the high sintering temperature and short sintering time (~10 s).

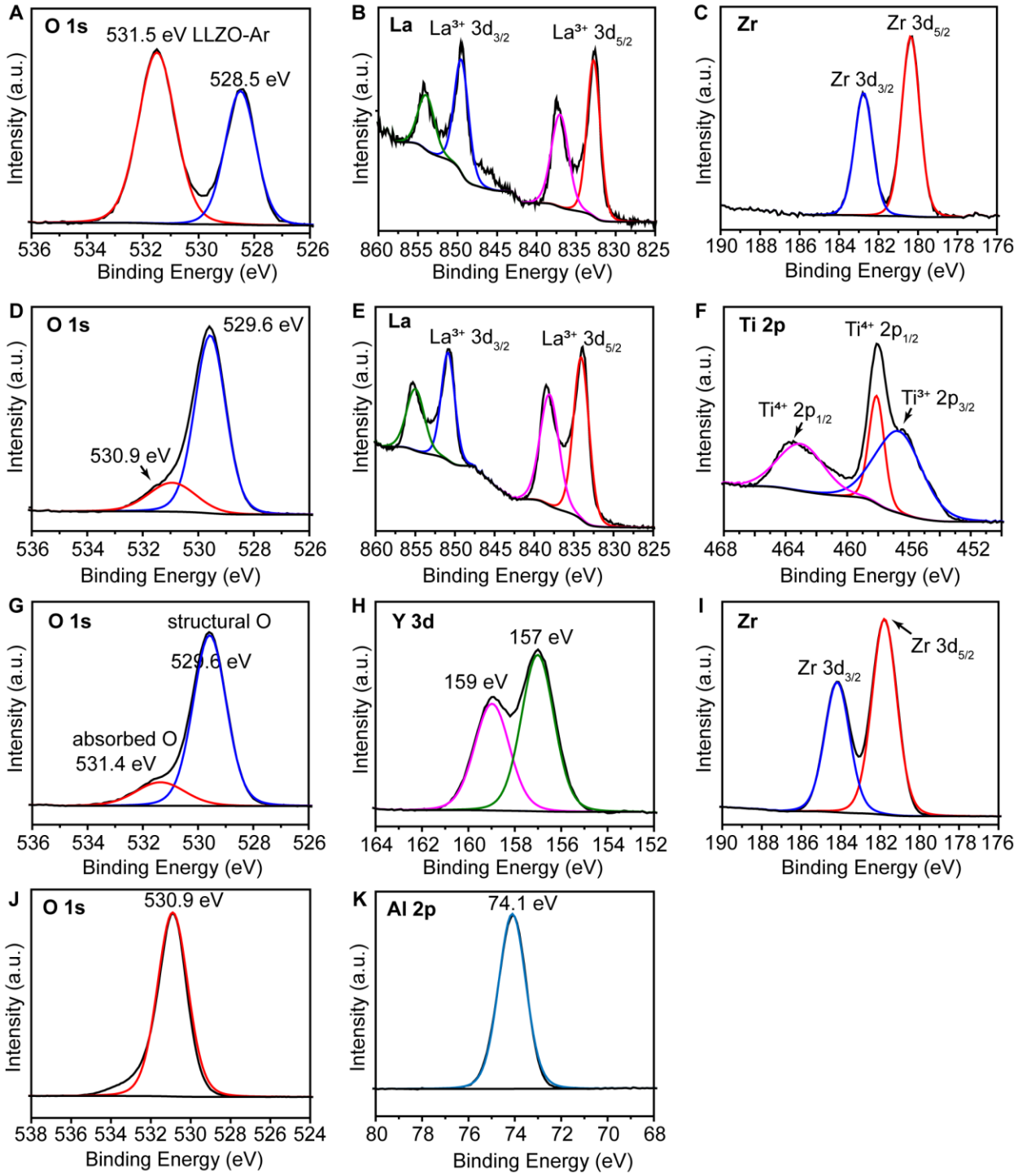

Figure S15. The XPS spectra of the main elements in pellets of LLZTO, LLTO, YSZ, and Al_2O_3 sintered by UHS. (A) O 1s, (B) La 3d, and (C) Zr 3d in LLZTO. (D) O 1s, (E) La 3d, and (F) Ti 2p in LLTO. (G) O 1s, (H) Y 3d, and (I) Zr 3d in YSZ. (J) O 1s, (K) Al 2p in Al_2O_3.

To determine the charge states of the main elements in the sintered ceramic pellets, XPS tests were performed and collected in Figure S15. All the ceramic pellets were sintered in an Ar-filled glovebox and transferred for immediate characterization. The spectra of each sample is calibrated against the main C-C peak at 284.8 eV. Typical XPS spectra of the main elements in LLZTO garnet sintered by UHS are shown in Figure S15A-C. The narrow region scan of O1s in Figure R1A illustrates that the oxygen peak has a binding energy of 528.5 eV corresponding to the structural oxygen in sintered LLZTO. Another peak at the higher binding energy of 531.5 eV is attributed to lithium carbonate and the absorbed oxygen from the environment (*50, 51*). Figure R1B shows the La 3d core spectra of the sintered garnet pellet, corresponding to La^{3+} in LLZTO with no apparent shoulder peak. Similarly, Zr 3d narrow region scans exhibit dominant Zr^{4+} $3d_{3/2}$ and Zr^{4+} $3d_{5/2}$ peaks (Figure S15C). Therefore, oxygen deficiencies and metal reduction in the UHS-sintered LLZTO garnet are negligible.

The XPS spectra of the main elements in the LLTO pellet sintered by UHS are shown in Figure S15D-F. The major peak at 530 eV in the O1s spectrum corresponds to the LLTO crystal structure oxygen. Another peak at a higher binding energy (~531 eV) is attributed to oxygen vacancies (*52*). After sintering by UHS, the LLTO had a hint of gray color due to the existence of oxygen vacancies in the pellet. Similarly, the Ti 2p scans reveal small contributions from Ti^{3+} $2p_{3/2}$ in addition to the main Ti^{4+} $2p_{1/2}$ peaks, which indicate that the Ti^{4+} is also partly reduced (*53, 54*). According to the Ellingham diagram (Figure S16)**,** Ti^{4+} is relatively unstable and can be potentially reduced by carbon at high temperature during the sintering process. For the UHS sintered LLTO, a post-annealing in air may be necessary to recover the reduced Ti.

The XPS spectra of the charge states in the UHS-sintered YSZ pellet are shown in Figure S15G-I. The O1s scans exhibit two peaks. The binding energy at 529.6 eV corresponds to structural O^{2-}

from the sintered YSZ, and the other one at 531.4 eV is due to the absorbed oxygen from the environment. The Y 3d scans reveal the peaks at binding energy of 159 eV and 157 eV are from sintered YSZ pellet. As shown in Figure R1I, the Zr $3d_{3/2}$ and Zr $3d_{5/2}$ peaks confirmed the Zr^{4+} state in the UHS-sintered YSZ pellet (*51, 55*). Therefore, the UHS sintered YSZ does not have any oxygen deficiencies or reduction issues.

The O1s scans in Figure S15J reveal the domain O^{2-} peak at a binding energy of 530.9 eV from the sintered Al_2O_3 pellet. Similarly, the Al 2p scans exhibit a single peak located at 74.1 eV from the sintered Al_2O_3 pellet (Figure S15K). Therefore, the UHS sintered Al_2O_3 do not have any obvious oxygen deficiencies or reduction issues.

In conclusion, due to the short sintering time of the UHS process, the deficiency of oxygen in the tested pellets is relatively small and often negligible. At the very least, these initial results indicate that under tuned conditions, the UHS technique is not any more susceptible to the formation of oxygen deficiencies during the sintering. It is possible to maintain the desire stoichiometry of the sample for most oxide ceramics.

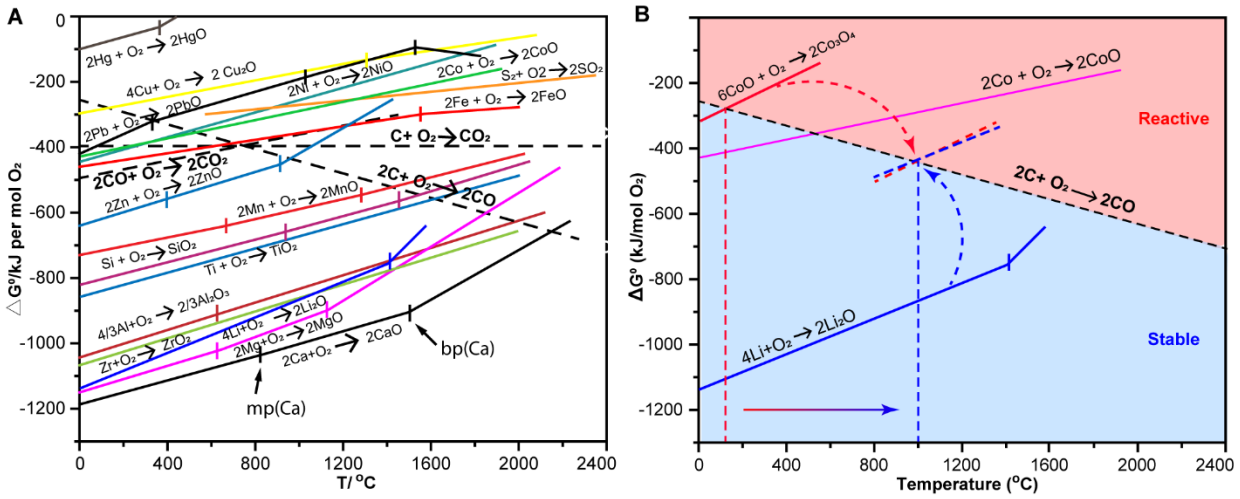

Figure S16. Ellingham diagram. (A) According the diagram, the negative slope of the Gibbs free energy curve of CO indicates that oxides can be reduced to metal by carbon as the temperature increases. However, because of the ultra-fast heating (~10^3–10^4 ℃/min) and cooling (up to 10^4 ℃/min) rates, as well as the short sintering time (1–10 s) of the UHS process, the ceramics can still be successfully synthesized with pure phase even at temperatures higher than their reduction temperature. (B) For example, even though pure Co_3O_4 can be potentially reduced by the carbon heater at ~200 ℃, according to the Ellingham diagram, we are still able to synthesize $LiCoO_2$ from Li_2CO_3 and Co_3O_4 precursors at a temperature of 1,000 ℃ via the UHS technique without the reduction of Co.

The high sintering temperature and short processing time of the UHS technique enables the synthesis of reactive materials without side reactions. According to the Ellingham diagram shown in Fig. S16, the standard reaction Gibbs free energy curve of carbon monoxide (CO) has a negative slope, which means some oxides can be potentially reduced by the carbon heater as the temperature increases. However, since many ceramics contain more than one type of oxide, the addition of other components can form new phases or compounds, which may be more stable or have lower sintering temperatures. For example, even though pure Co_3O_4 can be potentially reduced by carbon at temperatures greater than 200 ℃, we can still synthesize $LiCoO_2$ cathode material from Li_2CO_3 and Co_3O_4 precursors at a temperature of 1,000 ℃ via the UHS technique (Fig. S16B) without the reduction reaction of Co (Fig. S17). We hypothesize that the stable molten Li_2CO_3 (melting point: 723 ℃) protects Co_3O_4 and facilitates the reaction and sintering process, while the short sintering time can kinetically minimize the side reaction. Considering that most common oxides used in ceramics, including ZrO_2, Al_2O_3, TiO_2, SiO_2, CaO, and Li_2O, have lower standard reaction Gibbs free energies than CO at high temperatures up to 1,600 ℃ (Fig. S16), the UHS technique can be used to sinter a wide range of ceramic materials.

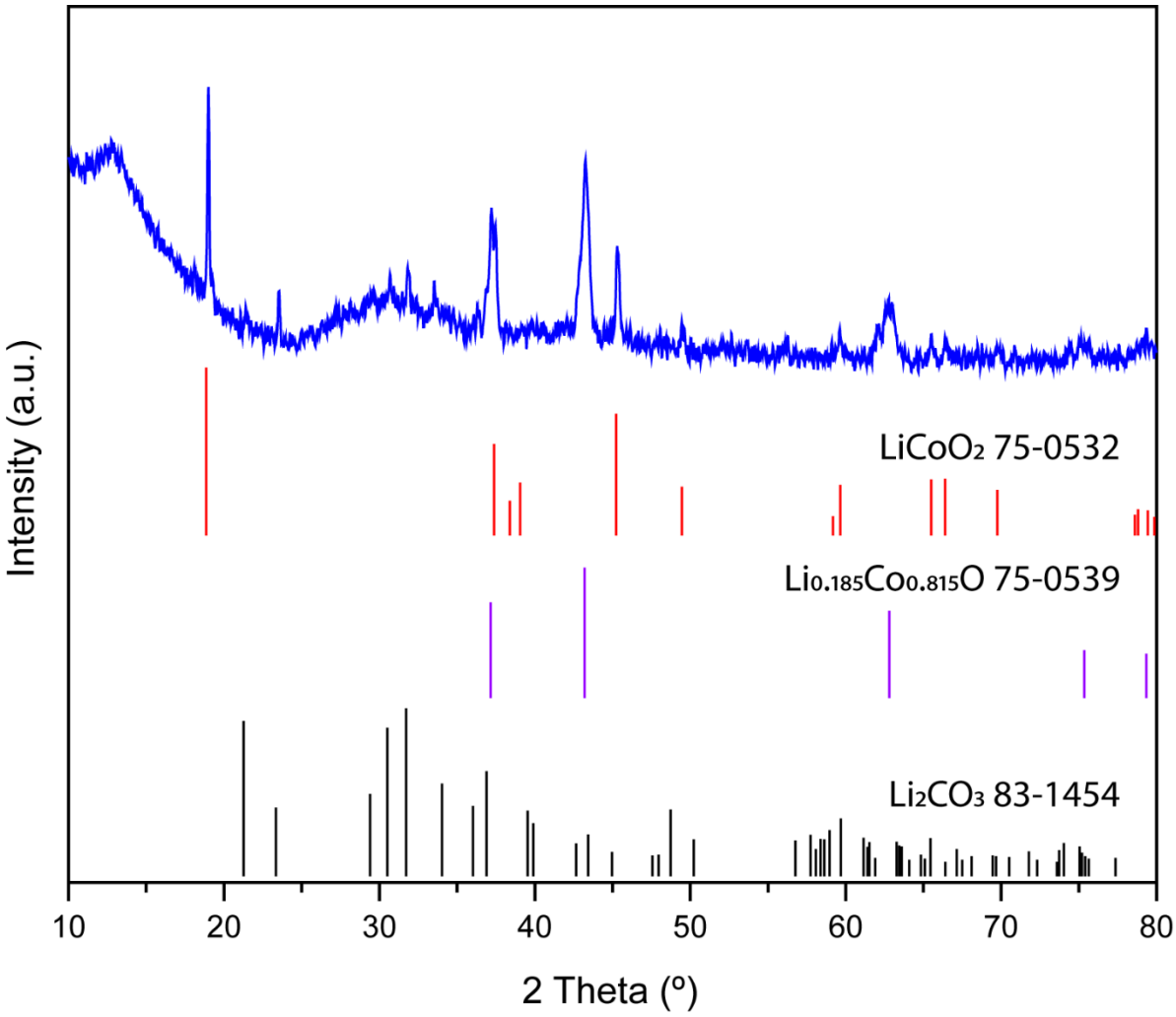

Figure S17. XRD of the UHS-synthesized $LiCoO_2$ from Li_2CO_3 and Co_3O_4 precursors at a temperature of 1,000 ℃. No Co reduction was observed, possibly due to the ultrafast sintering process (< 5 s) enabled by the UHS technique.

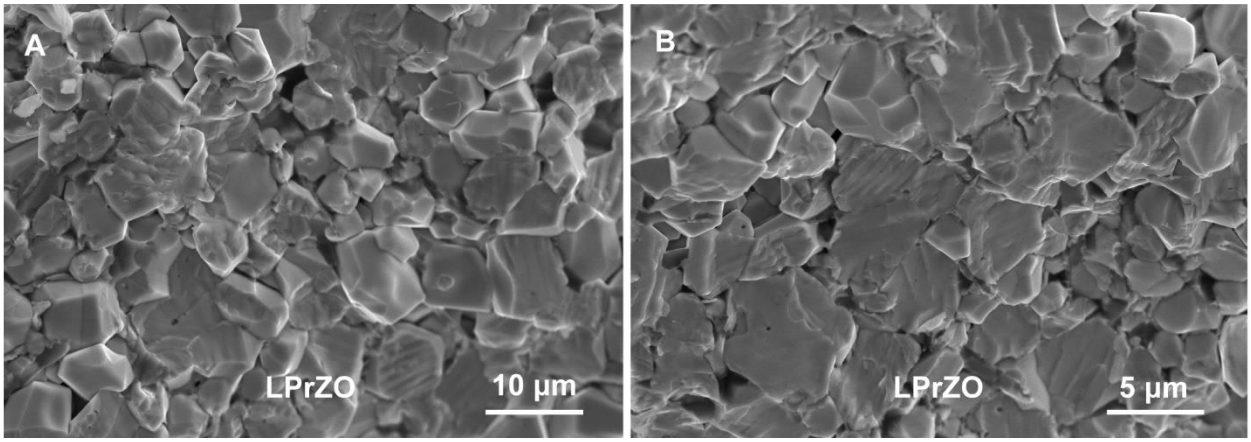

Figure S18. SEM images of the UHS-sintered $Li_7Pr_3Zr_2O_{12}$ (LPrZO) garnet pellet. (A) Cross-sectional SEM image and (B) a magnified view of the UHS-sintered LPrZO garnet pellet. This newly predicted garnet composition was well sintered by the UHS technique directly from the material precursors in one step, with relative densities above 96%.

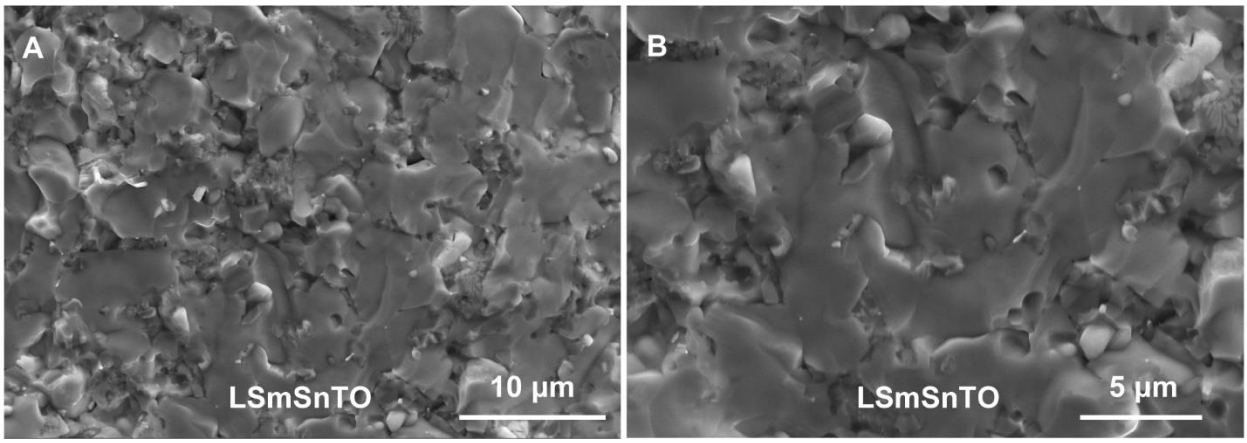

Figure S19. SEM images of the UHS-sintered $Li_{6.5}Sm_3Sn_{1.5}Ta_{0.5}O_{12}$ (LSmSnTO) garnet pellet. (A) Cross-sectional SEM image and (B) magnified view of the UHS-sintered LSmSnTO garnet pellet, which demonstrates well-merged grain boundaries, with relative densities above 92%. This newly predicted garnet composition was well sintered by the UHS technique directly from the material precursors in one step.

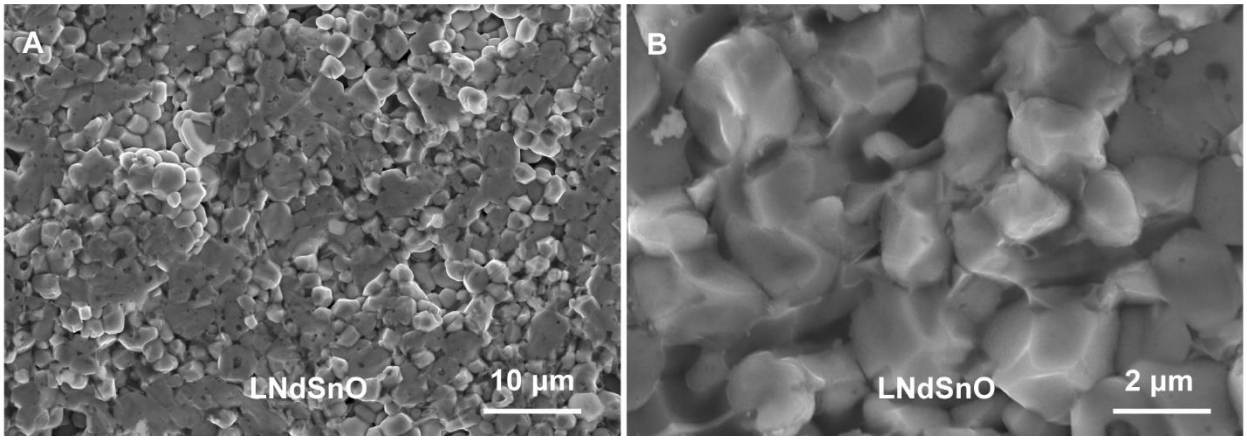

Figure S20. SEM images of the UHS-sintered $Li_7Nd_3Sn_2O_{12}$ (LNdSnO) garnet pellet. (A) Cross-sectional SEM image and (B) magnified view of the UHS-sintered LNdSnO garnet pellet, featuring uniform grain size. This newly predicted garnet composition was well sintered by the UHS technique directly from the material precursors in one step, with relative densities above 94%.

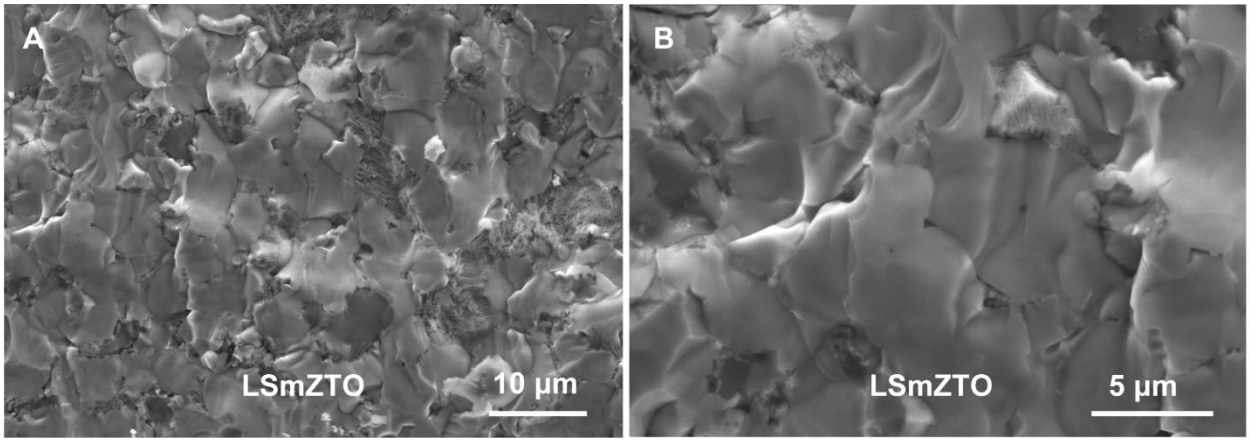

Figure S21. SEM images of the UHS-sintered $Li_{6.5}Sm_3Zr_{1.5}Ta_{0.5}O_{12}$ (LSmZTO) garnet pellet. (A) Cross-sectional SEM image and (B) magnified view of the UHS-sintered LSmZTO garnet pellet, featuring well-merged grain boundaries, with relative densities above 91%. This newly predicted garnet composition was well sintered by the UHS technique directly from the material precursors in one step.

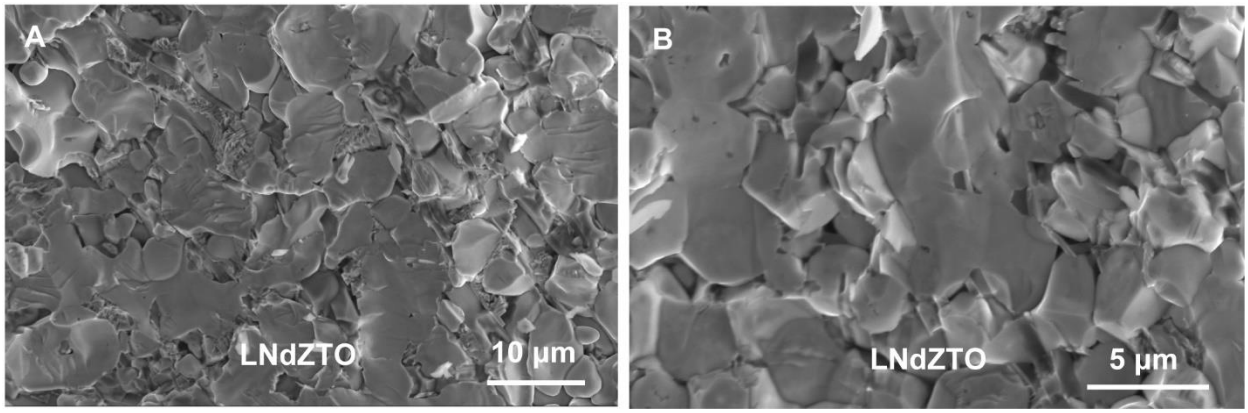

Figure S22. SEM images of the UHS-sintered $Li_{6.5}Nd_3Zr_{1.5}Ta_{0.5}O_{12}$ (LNdZTO) garnet pellet. (A) Cross-sectional SEM image and (B) magnified view of the UHS-sintered LNdZTO garnet pellet, featuring well-merged grain boundaries, with relative densities above 92%. This garnet composition was well sintered by the UHS technique directly from the material precursors in one step.

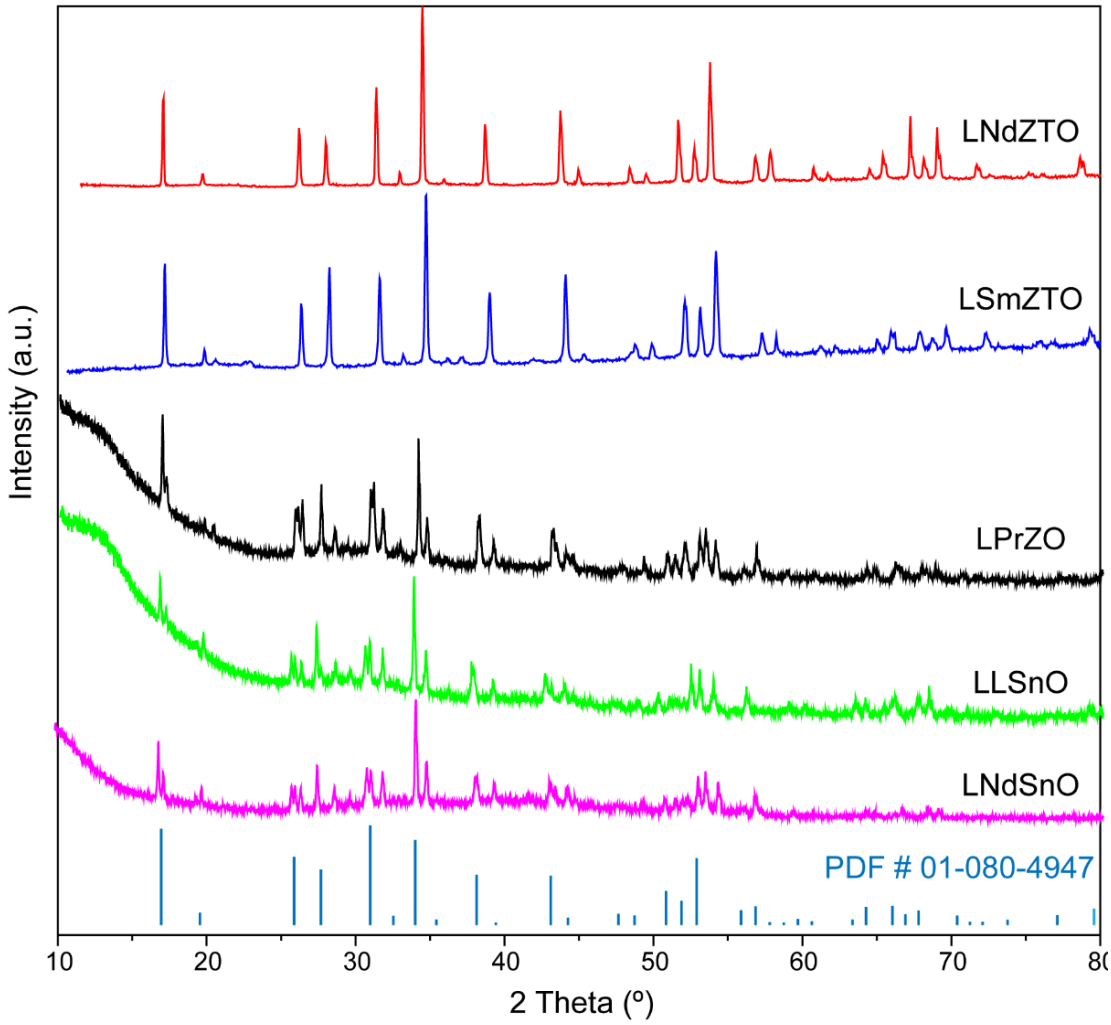

Figure S23. XRD patterns of the newly predicted garnet materials synthesized by the UHS technique directly from the material precursors in one step. The Ta-doped garnets (LNdZTO, LSmZTO) are cubic phase, while the undoped materials are tetragonal phase. Different compositions cause slight peak shifts to the high angle, indicating the shrinkage of the lattice. However, all the compositions demonstrate garnet phases.

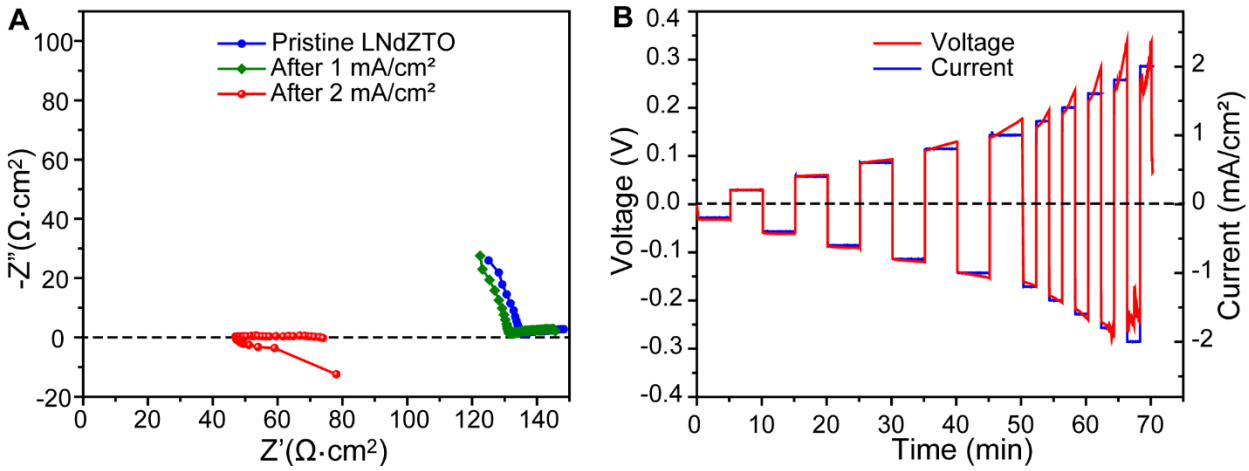

Figure S24. Electrochemical performance of the UHS-sintered LNdZTO ($Li_{6.5}Nd_3Zr_{1.5}Ta_{0.5}O_{12}$) garnet with a thickness of 0.5 mm. (A) EIS measurement of the Li-LNdZTO-Li symmetric cell before and after cycling at different current densities. The ionic conductivity was calculated to be ~3.8×10^{-4} S/cm, which is comparable to that of LLZO garnets (*18*, *23*). (B) The current and voltage profiles of the Li-LNdZTO-Li symmetric cell. The sudden voltage drop at a current density of 2 mA/cm^2 indicates the formation of a short-circuit. A critical current density of 2 mA/cm^2 is among the highest reported in the literature for garnet-based SSEs (*18*, *29*), indicating the excellent electrochemical stability of the new LNdZTO garnet SSE.

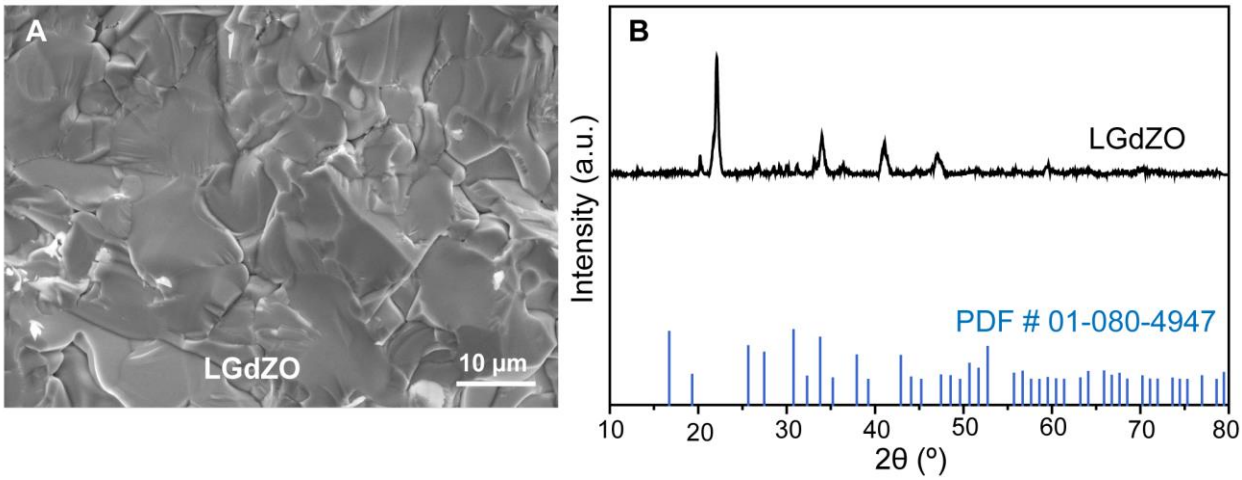

Figure S25. UHS-sintered unstable garnet composition predicted by computation. (A) Cross-sectional SEM image of the UHS-sintered $Li_7Gd_3Zr_2O_{12}$ (LGdZO), demonstrating the well-sintered grains. (B) XRD pattern of the UHS-sintered LGdZO, which do not feature garnet structures. These results agree with the computational predictions.

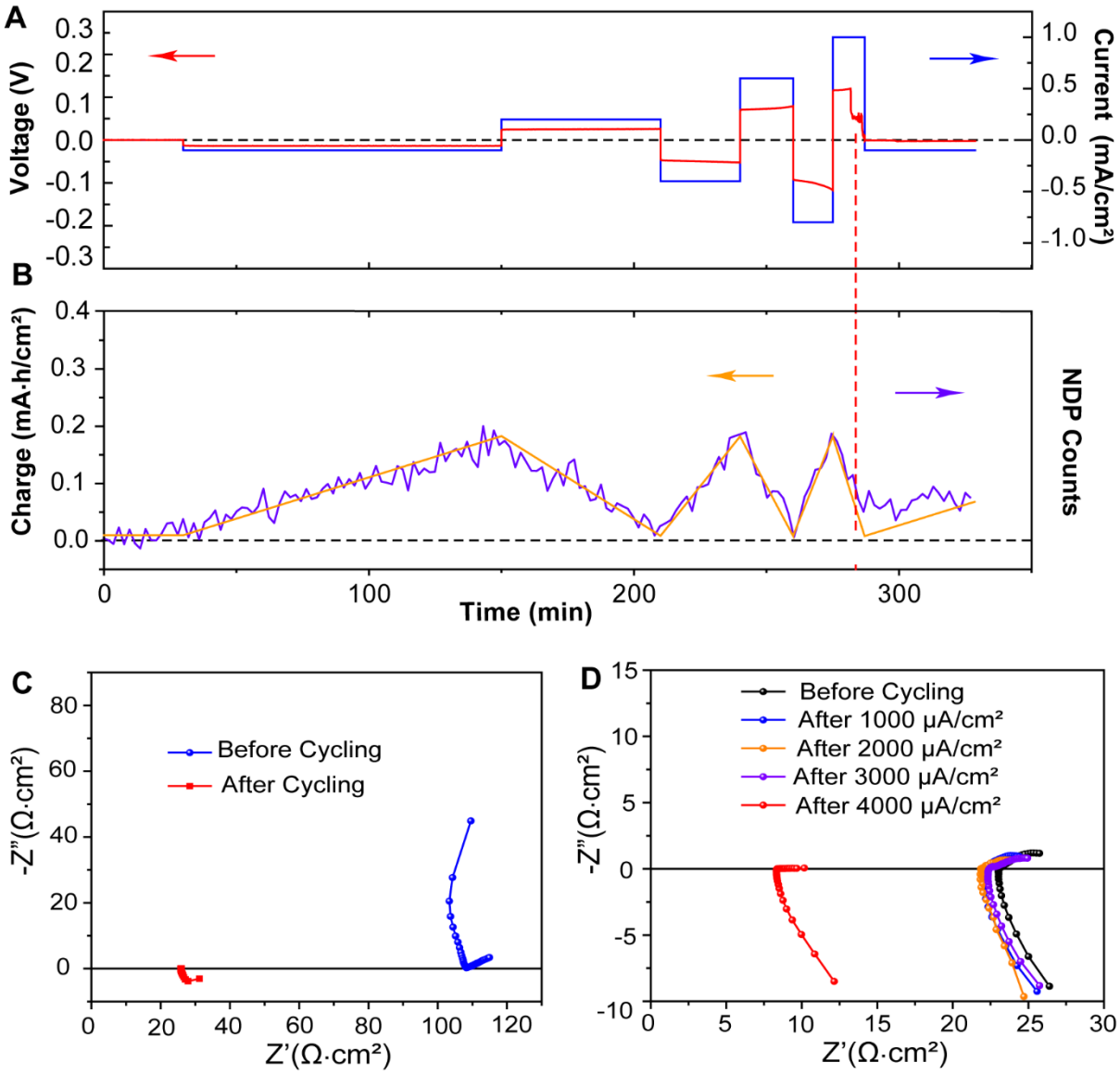

Figure S26. Electrochemical performance of the UHS-sintered LLZTO garnet SSE. (A) Voltage (red) and current (blue) profiles of symmetric cells made with UHS-LLZTO garnet cycled at different current densities for *in situ* NDP measurement. (B) The corresponding charge (green) and NDP count (purple) curves of the NDP cells. (C) EIS measurement of the symmetric cell made with the UHS-sintered LLZTO garnet SSE for the NDP measurements, in which the lowest point on the real axis indicates the overall resistance of the symmetric cell before cycling. (D) EIS measurement of the Li-LLZTO-Li symmetric cell with a thick (> 100 μm) Li metal coating and

the UHS-sintered LLZTO garnet after being cycled at different current densities. The stable resistance before 4000 μA/cm^2 confirms no short-circuiting.

We applied *in situ* neutron depth profiling (NDP)(*28*) to quantitatively monitor Li transport and confirm that the UHS LLZTO garnet SSE can conduct Li ions at high current densities without short-circuiting. We conducted the Li plating-stripping measurement of the Li-LLZTO-Li symmetric cell and achieved a critical current density as high as 1 mA/cm^2 (Fig. S26A), which we confirmed by the perfect match of the NDP curve and the charge curve (Fig. S26B) (*28*). In this measurement, the Li metal electrode was intentionally coated thin (~2-5 μm) on the garnet surface to achieve better NDP signal, which may have resulted in contact issues between the Li and garnet that prevented optimal performance. Therefore, we fabricated another symmetric cell with a thicker (> 100 μm) Li metal coating and found the critical current density was as high as 3.2 mA/cm^2 (Fig. 3G), which is among the highest reported values for planar garnet based SSEs (*18*, *29*).

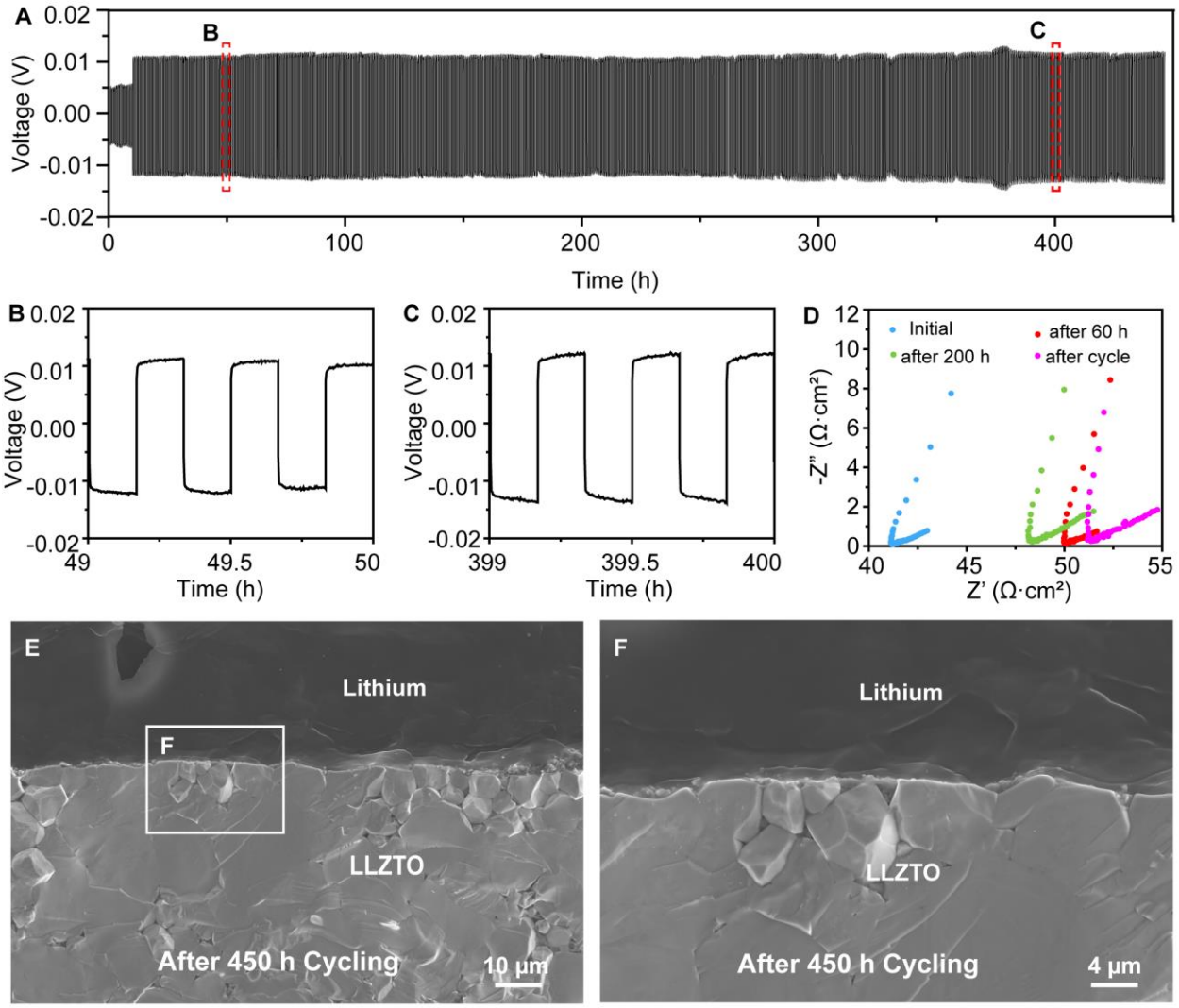

Figure S27. Cycling stability of the Li-UHS-sintered LLZTO-Li symmetric cell. (A) Voltage profile and (B, C) the zoomed-in voltage profiles of the symmetric cell cycled at current densities of 0.1 mA/cm^2 and 0.2 mA/cm^2. (D) Impedance resistance spectrum of the Li-UHS-sintered LLZTO-Li symmetric cell before cycling, after 60 h cycling, after 200 h cycling and after 450 h cycling. (E, F) The morphology of the interface of Li/UHS-sintered LLZTO after 450 h cycling.

We have conducted long-term cycling to characterize the cycling stability of the UHS-sintered LLZTO (Fig. S27). The Li-LLZTO-Li symmetric cells made with UHS-sintered LLZTO pellets can successfully cycle for more than 400 hours at a current density of 0.2 mA/cm^2, indicating the excellent cycling stability. The prolonged cycling time and stable cycling curve with small

polarization further prove the low interfacial resistance and stable interface contact between Li and UHS-sintered LLZTO. The EIS curves measured at different times during cycling is shown in Fig. S27D. The initial resistance of the symmetric cell is ~41 $\Omega \cdot cm^2$, which increase a little to ~50 $\Omega \cdot cm^2$ after 450 h cycling, illustrating the excellent stability of the interface of Li/sintered LLZTO. The small resistance changes can be due to the varication of the environmental temperature. The cross-sectional SEM images of the cycled pellets do not have any obvious changes in microstructures (Fig. S27, E and F). Therefore, the UHS-sintered LLZTO garnet demonstrates excellent electrochemical performance.

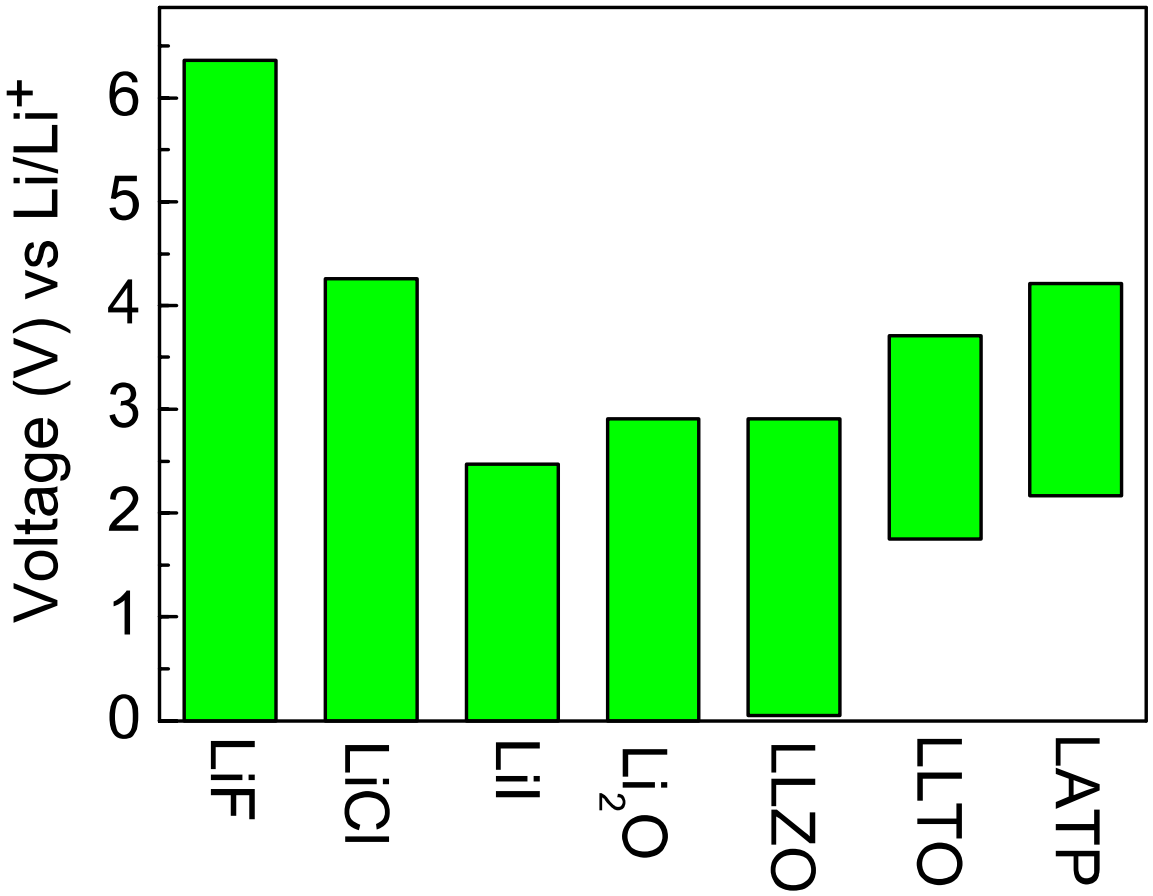

Figure S28. The stable electrochemical windows of lithium ionic conductors. Modified from reference (*30*).

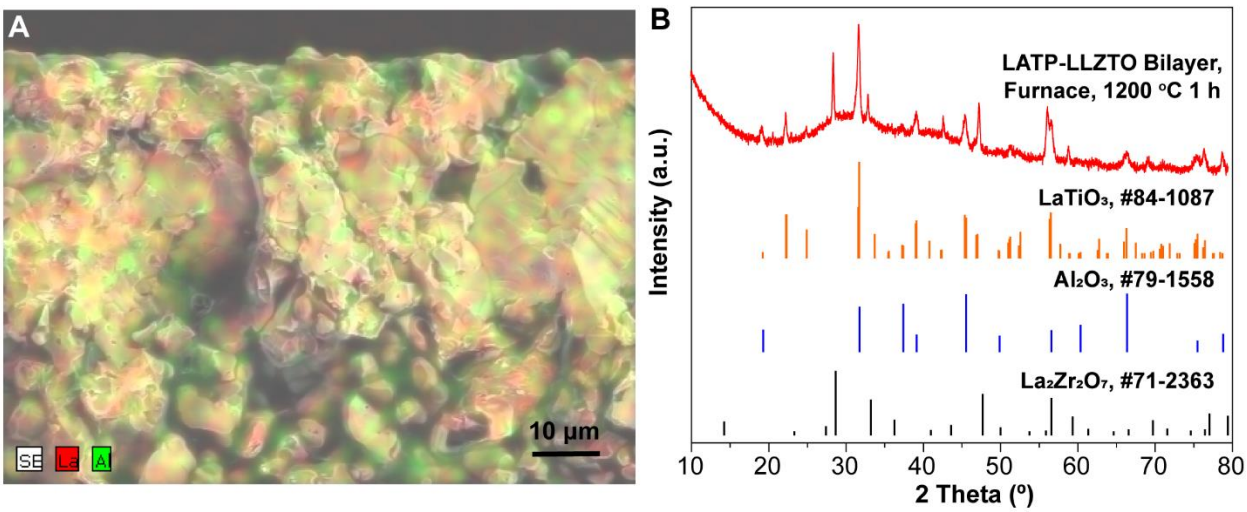

Figure S29. An LATP-coated LLZTO bilayer SSE sintered in a conventional furnace at 1,200 ℃ for 1 h. (A) EDS mapping of the LATP-LLZTO bilayer SSE sintered in a regular furnace, in which severe cross-doping is observed. The LATP coating layer has already diffused into the LLZTO bulk. (B) XRD pattern of the conventional furnace sintered LATP-LLZTO bilayer SSE. No original LATP or LLZTO phases can be identified, indicating severe side reactions.

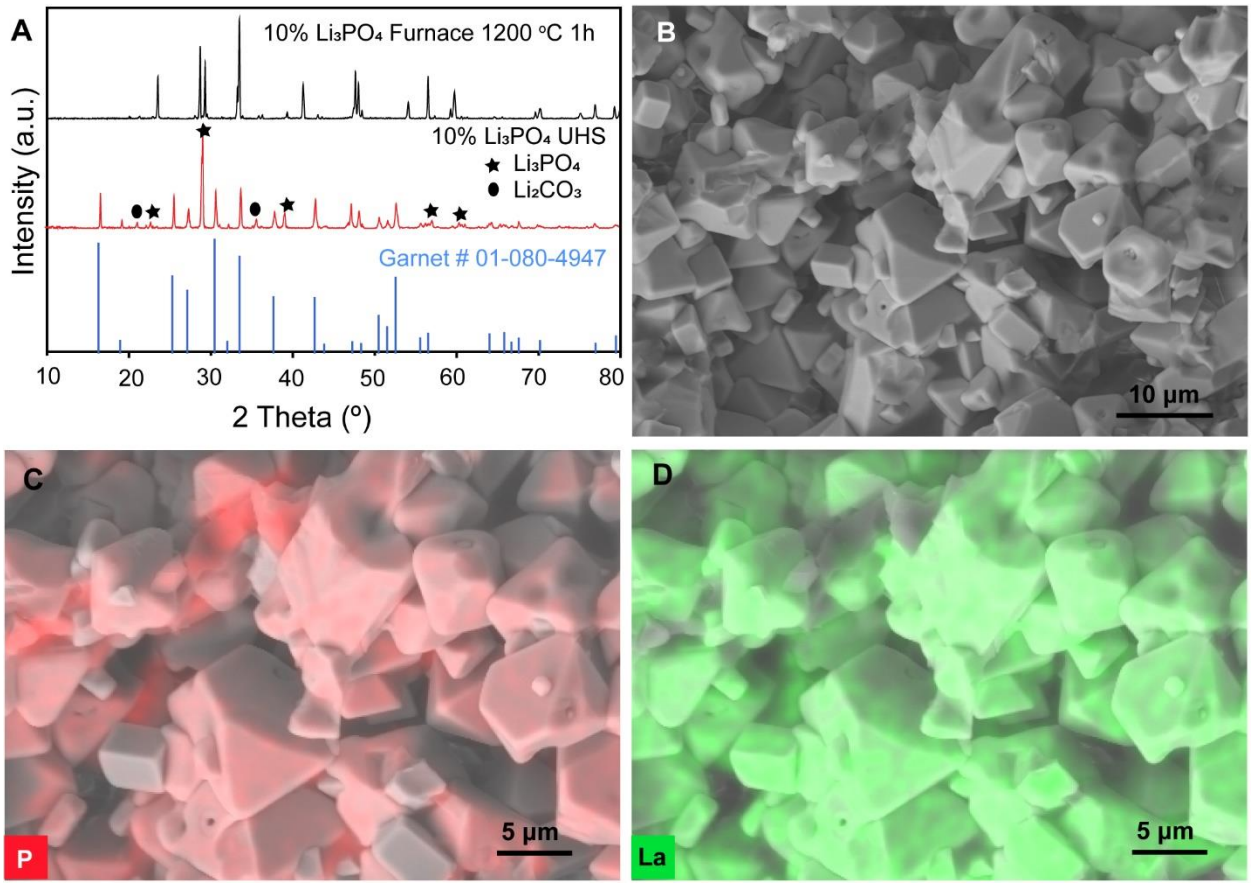

Figure S30. Li_3PO_4-LLZTO ($Li_{6.5}La_3Zr_{1.5}Ta_{0.5}O_{12}$) glass-ceramic composite achieved by the UHS technique without side reactions due to the short sintering time (10 s). (A) The XRD patterns of the UHS-sintered and conventional furnace sintered Li_3PO_4-LLZTO composite. The UHS-sintered composite still maintains the two pristine phases without side reactions, while the sample sintered in a conventional furnace exhibits nearly none of the original glass and garnet phases, indicating severe side reactions. Therefore, the UHS technique can be used to achieve multi-phase composite structures without cross-contamination. (B) SEM image and (C, D) EDS mapping of the 10 wt% Li_3PO_4-LLZTO composite sintered in a conventional furnace at 1,200 ℃ for 1 h, in which severe cross-doping can be observed.

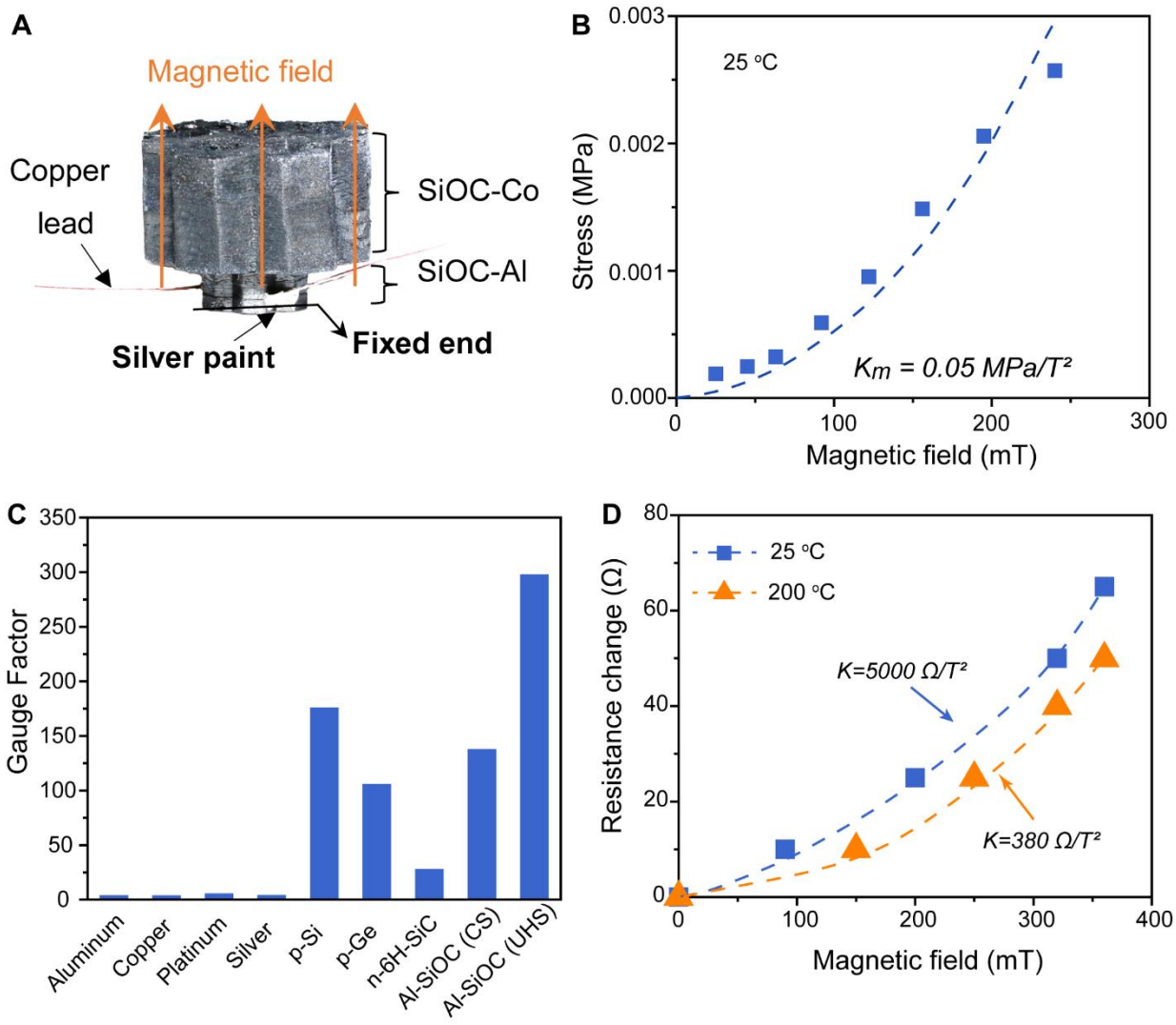

Figure S31. The UHS-sintered 3D printed multi-material magnetic flux density sensor. (A) Optical image of the fabricated multi-material magnetic flux density sensor. (B) The stress applied on the Al-doped SiOC section as a function of the magnetic field at 25 ℃. The stress is induced by the magnetic force of the Co-doped SiOC section. (C) Comparison of gauge factors of various materials, including Al-SiOC prepared by conventional sintering (CS) and UHS. (D) The resistance change of the Al-doped piezoresistive section as a function of the magnetic field.

To demonstrate the compatibility of the UHS process with 3D printing of multi-material structures, we fabricated a magnetic flux density sensor composed of a two-layer honeycomb

structure featuring 3D printed Al- and Co-doped SiOC, as shown in Fig. S31A. The piezoresistive component (Al-SiOC) correlates the applied stress and the resistance change (Fig. 4H), while the magnetic component (Co-SiOC) induces stress under a magnetic field (Fig. S31B). The piezoresistive properties of our 3D printed honeycomb structures prepared by conventional and UHS sintering are compared to previously reported state-of-the-art piezoresistive materials via the gauge factor (see Methods), as shown in Fig. S31C (*56*). We see a significant increase in the gauge factor for UHS sintering compared to conventional sintering and previous state-of-the-art materials. This establishes our rapid sintering technique as an innovative means to fabricate highly sensitive piezoresistive sensors that can be combined with magnetic materials for high-temperature magnetic field detection.

At 25 °C and 200 °C, a permanent magnet was used to generate magnetic fields ranging from 0 mT to 360 mT by varying the distance to the as-fabricated sensor, while a digital multimeter was used to read the resistance of the piezoresistive section of the sensor through two copper leads attached on both ends of the honeycomb structure. The resistance change of the sensor, ΔR, and the magnetic flux density, B, are correlated by,

$$\Delta R = KB^2$$

where K is the sensitivity of the sensor (more detail details can be found in the Methods). Fig. S31D shows the resistance change as a function of the applied magnetic field, and the sensitivity under 25 °C and 200 °C was derived through curve fitting.

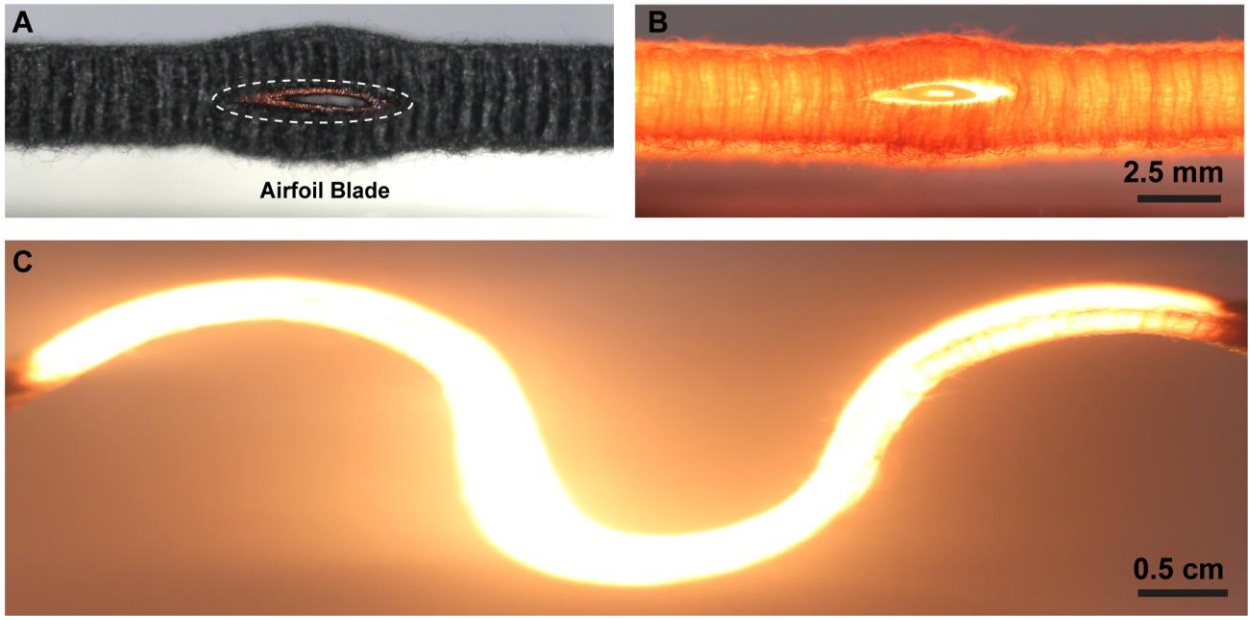

Figure S32. Photographs of carbon heater for conformal sintering of a 3D printed SiOC airfoil blade at (A) room temperature and (B) ~1,000 ℃. (C) A photograph of the carbon heater with an arbitrary shape at ~2,000 ℃.

Supplementary Movie Legends

Movie S1. Typical UHS process for rapid synthesis and sintering of LLZTO garnet SSE, with a moderate heating rate of ~20,000 °C/min (~5 s, from RT to ~1,500 °C) and ~6 s sintering at ~1,500 °C.

Movie S2. Typical UHS process for rapid synthesis and sintering of 3D printed SiOC, with a heating rate of ~2,400 °C/min (~30 s, from RT to ~1,200 °C) and ~10 s sintering at ~1,200 °C.

References and Notes

1. P. B. Vandiver, O. Soffer, B. Klima, J. Svoboda, The origins of ceramic technology at Dolni Věstonice, Czechoslovakia. *Science* **246**, 1002–1008 (1989). doi:10.1126/science.246.4933.1002

2. E. M. Rabinovich, Preparation of glass by sintering. *J. Mater. Sci.* **20**, 4259–4297 (1985). doi:10.1007/BF00559317

3. Z. Zhang, Y. Shao, B. Lotsch, Y.-S. Hu, H. Li, J. Janek, L. F. Nazar, C.-W. Nan, J. Maier, M. Armand, L. Chen, New horizons for inorganic solid state ion conductors. *Energy Environ. Sci.* **11**, 1945–1976 (2018). doi:10.1039/C8EE01053F

4. A. Manthiram, X. Yu, S. Wang, Lithium battery chemistries enabled by solid-state electrolytes. *Nat. Rev. Mater.* **2**, 16103 (2017). doi:10.1038/natrevmats.2016.103

5. Y. Li, J. T. Han, C. A. Wang, H. Xie, J. B. Goodenough, Optimizing Li+ conductivity in a garnet framework. *J. Mater. Chem.* **22**, 15357–15361 (2012). doi:10.1039/c2jm31413d

6. M. Nyman, T. M. Alam, S. K. McIntyre, G. C. Bleier, D. Ingersoll, Alternative approach to increasing Li mobility in Li-La-Nb/Ta garnet electrolytes. *Chem. Mater.* **22**, 5401–5410 (2010). doi:10.1021/cm101438x

7. I. Garbayo, M. Struzik, W. J. Bowman, R. Pfenninger, E. Stilp, J. L. M. Rupp, Glass-Type Polyamorphism in Li-Garnet Thin Film Solid State Battery Conductors. *Adv. Energy Mater.* **8**, 1702265 (2018). doi:10.1002/aenm.201702265

8. X. Huang, Y. Lu, Z. Song, K. Rui, Q. Wang, T. Xiu, M. E. Badding, Z. Wen, Manipulating Li2O atmosphere for sintering dense Li7La3Zr2O12 solid electrolyte. *Energy Storage Mater.* **22**, 207–217 (2019). doi:10.1016/j.ensm.2019.01.018

9. R. Pfenninger, M. Struzik, I. Garbayo, E. Stilp, J. L. M. Rupp, A low ride on processing temperature for fast lithium conduction in garnet solid-state battery films. *Nat. Energy* **4**, 475–483 (2019). doi:10.1038/s41560-019-0384-4

10. R. R. Mishra, A. K. Sharma, Microwave-material interaction phenomena: Heating mechanisms, challenges and opportunities in material processing. *Compos. Part A Appl. Sci. Manuf.* **81**, 78–97 (2016). doi:10.1016/j.compositesa.2015.10.035

11. M. Oghbaei, O. Mirzaee, Microwave versus conventional sintering: A review of fundamentals, advantages and applications. *J. Alloys Compd.* **494**, 175–189 (2010). doi:10.1016/j.jallcom.2010.01.068

12. O. Guillon, J. Gonzalez-Julian, B. Dargatz, T. Kessel, G. Schierning, J. Räthel, M. Herrmann, Field-assisted sintering technology/spark plasma sintering: Mechanisms, materials, and technology developments. *Adv. Eng. Mater.* **16**, 830–849 (2014). doi:10.1002/adem.201300409

13. M. Cologna, B. Rashkova, R. Raj, Flash sintering of nanograin zirconia in <5 s at 850°C. *J. Am. Ceram. Soc.* **93**, 3556–3559 (2010). doi:10.1111/j.1551-2916.2010.04089.x

14. D. Angmo, T. T. Larsen-Olsen, M. Jørgensen, R. R. Søndergaard, F. C. Krebs, Roll-to-roll inkjet printing and photonic sintering of electrodes for ITO free polymer solar cell

modules and facile product integration. *Adv. Energy Mater.* **3**, 172–175 (2013). doi:10.1002/aenm.201200520

15. Y. Zhang, J. Nie, J. M. Chan, J. Luo, Probing the densification mechanisms during flash sintering of ZnO. *Acta Mater.* **125**, 465–475 (2017). doi:10.1016/j.actamat.2016.12.015

16. M. Yu, S. Grasso, R. Mckinnon, T. Saunders, M. J. Reece, Review of flash sintering: Materials, mechanisms and modelling. *Adv. Appl. Ceramics* **116**, 24–60 (2017). doi:10.1080/17436753.2016.1251051

17. A. Albrecht, A. Rivadeneyra, A. Abdellah, P. Lugli, J. F. Salmerón, Inkjet printing and photonic sintering of silver and copper oxide nanoparticles for ultra-low-cost conductive patterns. *J. Mater. Chem. C* **4**, 3546–3554 (2016). doi:10.1039/C6TC00628K

18. V. Thangadurai, S. Narayanan, D. Pinzaru, Garnet-type solid-state fast Li ion conductors for Li batteries: Critical review. *Chem. Soc. Rev.* **43**, 4714–4727 (2014). doi:10.1039/c4cs00020j Medline

19. W. Ji, B. Parker, S. Falco, J. Y. Zhang, Z. Y. Fu, R. I. Todd, Ultra-fast firing: Effect of heating rate on sintering of 3YSZ, with and without an electric field. *J. Eur. Ceram. Soc.* **37**, 2547–2551 (2017). doi:10.1016/j.jeurceramsoc.2017.01.033

20. A. Sharafi, C. G. Haslam, R. D. Kerns, J. Wolfenstine, J. Sakamoto, Controlling and correlating the effect of grain size with the mechanical and electrochemical properties of Li7La3Zr2O12 solid-state electrolyte. *J. Mater. Chem. A* **5**, 21491–21504 (2017). doi:10.1039/C7TA06790A

21. R. P. Rao, W. Gu, N. Sharma, V. K. Peterson, M. Avdeev, S. Adams, In situ neutron diffraction monitoring of Li7La3Zr2O12 formation: Toward a rational synthesis of garnet solid electrolytes. *Chem. Mater.* **27**, 2903–2910 (2015). doi:10.1021/acs.chemmater.5b00149

22. E. Yi, W. Wang, J. Kieffer, R. M. Laine, Flame made nanoparticles permit processing of dense, flexible, Li + conducting ceramic electrolyte thin films of cubic-Li 7 La 3 Zr 2 O 12 (c-LLZO). *J. Mater. Chem. A* **4**, 12947–12954 (2016). doi:10.1039/C6TA04492A

23. Y. Jin, K. Liu, J. Lang, D. Zhuo, Z. Huang, C. Wang, H. Wu, Y. Cui, An intermediate temperature garnet-type solid electrolyte-based molten lithium battery for grid energy storage. *Nat. Energy* **3**, 732–738 (2018). doi:10.1038/s41560-018-0198-9

24. J. C. Bachman, S. Muy, A. Grimaud, H.-H. Chang, N. Pour, S. F. Lux, O. Paschos, F. Maglia, S. Lupart, P. Lamp, L. Giordano, Y. Shao-Horn, Inorganic Solid-State Electrolytes for Lithium Batteries: Mechanisms and Properties Governing Ion Conduction. *Chem. Rev.* **116**, 140–162 (2016). doi:10.1021/acs.chemrev.5b00563 Medline

25. G. Bernard-Granger, N. Benameur, C. Guizard, M. Nygren, Influence of graphite contamination on the optical properties of transparent spinel obtained by spark plasma sintering. *Scr. Mater.* **60**, 164–167 (2009). doi:10.1016/j.scriptamat.2008.09.027

26. S. P. Ong, L. Wang, B. Kang, G. Ceder, Li - Fe - P - O2 phase diagram from first principles calculations. *Chem. Mater.* **20**, 1798–1807 (2008). doi:10.1021/cm702327g

27. P. Albertus, S. Babinec, S. Litzelman, A. Newman, Status and challenges in enabling the lithium metal electrode for high-energy and low-cost rechargeable batteries. *Nat. Energy* **3**, 16–21 (2018). doi:10.1038/s41560-017-0047-2

28. C. Wang, Y. Gong, J. Dai, L. Zhang, H. Xie, G. Pastel, B. Liu, E. Wachsman, H. Wang, L. Hu, In Situ Neutron Depth Profiling of Lithium Metal-Garnet Interfaces for Solid State Batteries. *J. Am. Chem. Soc.* **139**, 14257–14264 (2017). doi:10.1021/jacs.7b07904 Medline

29. N. J. Taylor, S. Stangeland-Molo, C. G. Haslam, A. Sharafi, T. Thompson, M. Wang, R. Garcia-Mendez, J. Sakamoto, Demonstration of high current densities and extended cycling in the garnet Li7La3Zr2O12 solid electrolyte. *J. Power Sources* **396**, 314–318 (2018). doi:10.1016/j.jpowsour.2018.06.055

30. Y. Zhu, X. He, Y. Mo, First principles study on electrochemical and chemical stability of solid electrolyte-electrode interfaces in all-solid-state Li-ion batteries. *J. Mater. Chem. A* **4**, 3253–3266 (2016). doi:10.1039/C5TA08574H

31. A. Bandyopadhyay, B. Heer, Additive manufacturing of multi-material structures. *Mater. Sci. Eng. Rep.* **129**, 1–16 (2018). doi:10.1016/j.mser.2018.04.001

32. R. Lakes, Cellular solids with tunable positive or negative thermal expansion of unbounded magnitude. *Appl. Phys. Lett.* **90**, 221905 (2007). doi:10.1063/1.2743951

33. X. Kuang, J. Wu, K. Chen, Z. Zhao, Z. Ding, F. Hu, D. Fang, H. J. Qi, Grayscale digital light processing 3D printing for highly functionally graded materials. *Sci. Adv.* **5**, eaav5790 (2019). doi:10.1126/sciadv.aav5790 Medline

34. I. P. Roof, M. D. Smith, E. J. Cussen, H. C. zur Loye, Crystal growth of a series of lithium garnets Ln3Li5Ta2O12 (Ln=La, Pr, Nd): Structural properties, Alexandrite effect and unusual ionic conductivity. *J. Solid State Chem.* **182**, 295–300 (2009). doi:10.1016/j.jssc.2008.10.032

35. Z. Liang, Y. Pei, C. Chen, B. Jiang, Y. Yao, H. Xie, M. Jiao, G. Chen, T. Li, B. Yang, L. Hu, General, Vertical, Three-Dimensional Printing of Two-Dimensional Materials with Multiscale Alignment. *ACS Nano* **13**, 12653–12661 (2019). doi:10.1021/acsnano.9b04202 Medline

36. S. H. Chen, S. C. Saxena, Thermal conductivity of argon in the temperature range 350 to 2500 k. *Mol. Phys.* **29**, 455–466 (1975). doi:10.1080/00268977500100391

37. P. E. Blöchl, Projector augmented-wave method. *Phys. Rev. B* **50**, 17953–17979 (1994). doi:10.1103/PhysRevB.50.17953 Medline

38. J. P. Perdew, K. Burke, M. Ernzerhof, Generalized gradient approximation made simple. *Phys. Rev. Lett.* **77**, 3865–3868 (1996). doi:10.1103/PhysRevLett.77.3865 Medline

39. G. Kresse, J. Furthmüller, Efficient iterative schemes for ab initio total-energy calculations using a plane-wave basis set. *Phys. Rev. B* **54**, 11169–11186 (1996). doi:10.1103/PhysRevB.54.11169 Medline

40. A. Jain, G. Hautier, C. J. Moore, S. Ping Ong, C. C. Fischer, T. Mueller, K. A. Persson, G. Ceder, A high-throughput infrastructure for density functional theory calculations. *Comput. Mater. Sci.* **50**, 2295–2310 (2011). doi:10.1016/j.commatsci.2011.02.023

41. S. P. Ong, W. D. Richards, A. Jain, G. Hautier, M. Kocher, S. Cholia, D. Gunter, V. L. Chevrier, K. A. Persson, G. Ceder, Python Materials Genomics (pymatgen): A robust, open-source python library for materials analysis. *Comput. Mater. Sci.* **68**, 314–319 (2013). doi:10.1016/j.commatsci.2012.10.028

42. Y. Zhu, X. He, Y. Mo, Origin of Outstanding Stability in the Lithium Solid Electrolyte Materials: Insights from Thermodynamic Analyses Based on First-Principles Calculations. *ACS Appl. Mater. Interfaces* **7**, 23685–23693 (2015). doi:10.1021/acsami.5b07517 Medline

43. S. Dudarev, G. Botton, S. Y. Savrasov, C. J. Humphreys, A. P. Sutton, Electron-energy-loss spectra and the structural stability of nickel oxide: An LSDA+U study. *Phys. Rev. B* **57**, 1505–1509 (1998). doi:10.1103/PhysRevB.57.1505

44. L. Pauling, The principles determining the structure of complex ionic crystals. *J. Am. Chem. Soc.* **51**, 1010–1026 (1929). doi:10.1021/ja01379a006

45. R. D. Shannon, Revised effective ionic radii and systematic studies of interatomic distances in halides and chalcogenides. *Acta Cryst.* **A32**, 751–767 (1976). doi:10.1107/S0567739476001551

46. H. Cui, R. Hensleigh, H. Chen, X. Zheng, Additive Manufacturing and size-dependent mechanical properties of three-dimensional microarchitected, high-temperature ceramic metamaterials. *J. Mater. Res.* **33**, 360–371 (2018). doi:10.1557/jmr.2018.11

47. D. Chen, X. Zheng, Multi-material Additive Manufacturing of Metamaterials with Giant, Tailorable Negative Poisson's Ratios. *Sci. Rep.* **8**, 9139 (2018). doi:10.1038/s41598-018-26980-7 Medline

48. Y. Cao, X. Yang, R. Zhao, Y. Chen, N. Li, L. An, Giant piezoresistivity in polymer-derived amorphous SiAlCO ceramics. *J. Mater. Sci.* **51**, 5646–5650 (2016). doi:10.1007/s10853-016-9866-y

49. A. L. Gassner, M. Abonnenc, H.-X. Chen, J. Morandini, J. Josserand, J. S. Rossier, J.-M. Busnel, H. H. Girault, Magnetic forces produced by rectangular permanent magnets in static microsystems. *Lab Chip* **9**, 2356–2363 (2009). doi:10.1039/b901865d Medline

50. Y. Li, X. Chen, A. Dolocan, Z. Cui, S. Xin, L. Xue, H. Xu, K. Park, J. B. Goodenough, Garnet Electrolyte with an Ultralow Interfacial Resistance for Li-Metal Batteries. *J. Am. Chem. Soc.* **140**, 6448–6455 (2018). doi:10.1021/jacs.8b03106 Medline

51. H. B. Wang, C. R. Xia, G. Y. Meng, D. K. Peng, Deposition and characterization of YSZ thin films by aerosol-assisted CVD. *Mater. Lett.* **44**, 23–28 (2000). doi:10.1016/S0167-577X(99)00291-8

52. Y. T. Chen, A. Jena, W. K. Pang, V. K. Peterson, H.-S. Sheu, H. Chang, R.-S. Liu, Voltammetric Enhancement of Li-Ion Conduction in Al-Doped Li7-xLa3Zr2O12 Solid Electrolyte. *J. Phys. Chem. C* **121**, 15565–15573 (2017). doi:10.1021/acs.jpcc.7b04004

53. K. Y. Yang, K. Z. Fung, M. C. Wang, X-ray photoelectron spectroscopic and secondary ion mass spectroscopic examinations of metallic-lithium-activated donor doping process on la 0.56Li0.33TiO3 surface at room temperature. *J. Appl. Phys.* **100**, 056102 (2006). doi:10.1063/1.2337787

54. A. Mei, Q. H. Jiang, Y. H. Lin, C. W. Nan, Lithium lanthanum titanium oxide solid-state electrolyte by spark plasma sintering. *J. Alloys Compd.* **486**, 871–875 (2009). doi:10.1016/j.jallcom.2009.07.091

55. S. D. Kim, H. Moon, S. Hyun, J. Moon, J. Kim, H. Lee, Performance and durability of Ni-coated YSZ anodes for intermediate temperature solid oxide fuel cells. *Solid State Ion.* **177**, 931–938 (2006). doi:10.1016/j.ssi.2006.02.007

56. A. S. Fiorillo, C. D. Critello, A. S. Pullano, Theory, technology and applications of piezoresistive sensors: A review. *Sens. Actuators A Phys.* **281**, 156–175 (2018). doi:10.1016/j.sna.2018.07.006